Thalamus drives two complementary input strata of the neocortex in parallel

R. Egger[1]†‡, R.T. Narayanan[1]†, D. Udvary[1], A. Bast[1], J.M. Guest[1], S. Das[2], C.P.J. de Kock[2], M. Oberlaender[1]*

[1]Max Planck Group: In Silico Brain Sciences, Center of Advanced European Studies and Research, Bonn, Germany; [2]Department of Integrative Neurophysiology, Center for Neurogenomics and Cognitive Research, VU Amsterdam, The Netherlands.

Short title: The deep input stratum of the neocortex

Key words: barrel cortex, pyramidal tract neurons, corticocortical neurons, whisker touch, in silico

† **these authors contributed equally** (in alphabetical order)

‡ current address: Neuroscience Institute, NYU School of Medicine, New York, USA.

* **Editorial correspondence:**
Max Planck Group: In Silico Brain Sciences
Center of Advanced European Studies and Research (caesar)
Ludwig-Erhard-Allee 2, Bonn, 53175 Germany
marcel.oberlaender@caesar.de

Sensory information enters the neocortex via thalamocortical axons that define the major 'input' layer 4. The same thalamocortical axons, however, additionally innervate the deep 'output' layers 5/6. How such bistratification impacts cortical processing remains unknown. Here, we find a class of neurons that cluster specifically around thalamocortical axons at the layer 5/6 border. We show that these *border stratum cells* are characterized by extensive horizontal axons, that they receive strong convergent input from the thalamus, and that this input is sufficient to drive reliable sensory-evoked responses, which precede those in layer 4. These cells are hence strategically placed to amplify and relay thalamocortical inputs across the cortical area, for example to drive the fast onsets of cortical output patterns. Layer 4 is therefore not the sole starting point of cortical processing. Instead, parallel activation of layer 4 and the border stratum is necessary to broadcast information out of the neocortex.

Introduction

The mammalian neocortex is required for higher-order brain functions, such as sensory perception and cognition, and hence for the transformation of information from the environment into behavior. Such information, for example as evoked by photo- or mechanoreceptor cells at the periphery of the visual or somatosensory system, enters the neocortex in form of a synchronous volley of excitation, which is provided by relay cells that are located in sensory system-specific primary nuclei of the thalamus [1]. Despite several species- and sensory system-specific differences, thalamocortical axons of relay cells terminate in general most densely in layer 4 of the respective primary sensory areas of the neocortex [2]. For decades, concepts about the neocortex thus focused on layer 4 as its main input site, and starting point of sensory information processing [3]. However, anatomical studies in macaques [4], cats [5], and rodents [6] indicate that the very same thalamocortical axons give rise to a second innervation peak at specific depth locations in the deeper layers 5 and/or 6. These layers represent the main output site of the neocortex, as they comprise long-range projection neurons that innervate subcortical brain structures [2].

The relevance of bistratified thalamocortical input for cortical information processing – and in particular of the deep input stratum within the output layers – remains poorly understood [7]. However, this knowledge is fundamental for deducing the logic of intracortical signal flow, for revealing the origin of cell type- and layer-specific neuronal activity patterns, and for constraining hypotheses of cortical circuit organization. So far, to our knowledge, no study has yet systematically investigated the principles by which a deep thalamocortical input stratum contributes to the overall sensory-evoked cortical excitation. It remains therefore unknown whether and how different types of neurons in the output layers can be driven directly by thalamocortical input, and if that would be the case, how responses in the deep input stratum affect those in the upper layers and vice versa.

Here, we address these questions in the whisker somatosensory system of the rat [8]. Tactile information from whisker touch enters the neocortex via relay cells from the ventral posterior medial nucleus (VPM) of the thalamus [2]. Axons from these relay cells delineate layer 4 of the whisker-related part of the primary somatosensory cortex (wS1). Within layer 4, excitatory spiny neurons cluster around the dense terminal fields of the VPM axons. Upon sensory stimulation, this major thalamorecipient population gives rise to recurrent excitation within layer 4 and feed-forward excitation to the superficial layers 2/3 – a canonical organizational principle of all sensory cortices [3]. VPM axons show a second, less dense innervation peak in the deeper layers [6]. The VPM-to-wS1 pathway in rodents hence represents an ideal model system to elucidate the relevance of bistratified thalamocortical input for cortical sensory information processing.

Combining *in vivo* recordings with morphological reconstructions, optogenetic input mappings, pharmacological manipulations, and simulations of cortical signal flow, we reveal that – similar to the organization of layer 4 – thalamocortical inputs converge strongly onto a population of corticocortical cells that is strategically placed around the terminal fields of VPM axons at the layer 5/6 border. Upon sensory stimulation, this deep thalamorecipient pathway is activated first, evoking a stream of excitation that spreads horizontally across the deep layers, and which thereby precedes the vertical stream of signal flow through the canonical layer 4 to layers 2/3 pathway. Neuronal responses in primary sensory cortices may thus be regarded as a superposition of inputs from two simultaneously active primary thalamocortical pathways, which likely complement each other to ensure that intracortical computations are reliably transformed into cortical output patterns.

Results

Corticocortical cells cluster around deep layer thalamocortical axons

We compared the soma, dendrite, and axon distributions of all major excitatory cortical cell types [2] with the distributions of thalamocortical axons, and precise measurements of the cytoarchitectonic layer borders **(Fig. S1)** – anatomical data that we had systematically collected for one set of experimental conditions over the past decade in rat VPM and wS1 [6, 9, 10, 11, 12, 13, 14]. The comparison revealed that the peak density of VPM axons in the deep layers coincides with the cytoarchitectonic border between layers 5 and 6 **(Fig. 1A)**. Moreover, the soma depth distribution of layer 6 corticocortical (i.e., intratelencephalic) neurons matches the vertical extent of the deep layer VPM axon density peak **(Fig. 1B)**. Neurons of this class are hence not restricted to layer 6, but equally abundant in lower layer 5 and upper layer 6.

These layer 5/6 corticocortical neurons can be easily distinguished from the subcortically projecting cortical output neurons that are found at the same depth: layer 5 pyramidal tract and layer 6 corticothalamic neurons. First, by the characteristic morphology of their apical dendrites **(Fig. 1C)**, which terminate in layer 4 without forming a tuft. This property also distinguishes them from polymorphic corticocortical neurons in deeper regions of layer 6 [12]. Second, by their extensive horizontally projecting axons **(Fig. 1D)**, which can span across the deep layers of the entire cortical area **(Fig. 1E)**. Our data reveal that analogously to the organization of excitatory populations in the major thalamorecipient layer, neurons with dendrite morphologies similar to those in layer 4, but with complementary intracortical axon projection patterns, cluster around thalamocortical axons in the deep layers. Together, VPM axons and layer 5/6 corticocortical neurons thus provide the structural basis of a deep thalamorecipient pathway for sensory-evoked signal flow, which we subsequently refer to as the '*layer 5/6 border stratum*' [4].

Thalamocortical inputs converge strongly onto border stratum cells

Functional and anatomical studies in the rodent somatosensory [7, 15] and visual systems [16] suggest that neurons of all excitatory cell types that are located at the depth of the border stratum can receive direct input from the respective primary thalamic nuclei. We therefore quantified the degree to which border stratum cells (i.e., layer 5/6 corticocortical) in rat wS1 form monosynaptic connections with VPM axons, and investigated whether these synapses are functional under *in vivo* conditions. We expressed light-gated ion channels and a fluorescent marker within the thalamocortical synapses by injecting an adeno-associated virus into the VPM **(Fig. 2A)**. Light-evoked and sensory-evoked action potential (AP) responses of individual wS1 neurons were obtained via cell-attached recordings in anesthetized rats **(Fig. 2B)**. Following the recordings, neurons were filled *in vivo* with biocytin, which allowed for post-hoc reconstruction and classification of the neurons' morphology **(Fig. 2C)**, and detection of the putative thalamocortical synapses along the dendrites of the recorded neurons **(Fig. 2D)**.

The experiments revealed that 7±2% of the spines along the dendrites of a border stratum cell receive input from the VPM **(Fig. 2E)**. Similar fractions (10±4%) and dendritic distributions of VPM synapses have been reported previously for spiny neurons in layer 4 of rat wS1 [17]. Thus, the excitatory populations that define the respective postsynaptic parts of the two thalamocortical input strata – layer 4 spiny neurons and layer 5/6 border stratum cells – receive similar relative amounts of VPM input. Supporting these anatomical observations, light stimulation of VPM synapses elicited APs in the morphologically identified border stratum cells. The responses were equally reliable and as fast as those in layer 4 spiny neurons **(Fig. 2F)**. The same border stratum cells also responded to sensory stimuli, as evoked by a low pressure airpuff that deflects all whiskers caudally. Under these conditions, sensory responses in border stratum cells were more reliable compared to those of spiny neurons in layer 4, and even rivaled the reliability of relay cells in the VPM **(Fig. 2G)**. Our data reveal that analogously to layer 4 **(Fig. S2)**, the strategic location of border stratum cells results in strong convergent input from primary thalamocortical axons, which provides the synaptic basis of a deep thalamorecipient pathway for sensory-evoked signal flow.

Border stratum cells respond first to sensory stimuli

Whole-cell recordings in rodent wS1 [18] and V1 [16] indicate that deep layer corticocortical neurons have intrinsic physiological properties that render them as highly excitable when compared to corticothalamic neurons that are found at the same depth. Together with our observation of strong convergence of thalamocortical axons, this suggests that synaptic input from these fibers may be sufficient to drive reliable sensory-evoked responses in border stratum cells (e.g. those shown in **Fig. 2G**). This hypothesis is supported by several studies which showed that response onsets (i.e., latency to first AP) of deep layer

neurons can rival, and even precede those in layer 4 [7, 10, 19]. To quantitatively test this hypothesis, we measured the additional path length between the border stratum and layer 4 that APs need to travel along VPM axons. Combined with conduction velocity measurements [20], the analysis predicted that sensory-evoked excitation reaches the border stratum 2 to 5 ms (3.0±1.7 ms) earlier than layer 4 **(Fig. 3A)**.

To test the prediction, we recorded and labeled excitatory neurons across all layers of wS1 in anesthetized rats. These experiments allowed to precisely control the stimulus onset by deflecting individual whiskers with a piezoelectric bimorph [10], and to recover the morphological cell type of the recorded neurons **(Fig. 3B)**. We found that responses in the deep layers to deflections of the whisker that was somatotopically aligned with the recording site – the principal whisker – were largely restricted to the populations of border stratum and pyramidal tract neurons **(Fig. S3)**. Similar to the multi-whisker stimulations by airpuff, single whisker deflections evoked AP responses that were more reliable in border stratum cells when compared to layer 4 neurons **(Fig. 3C)**. Response onsets of border stratum cells (median/25th/75th percentile: 11.2/10.3/12.4 ms) preceded those in all other excitatory cell types – including layer 4 – matching the path length-based delay predictions (14.3/13.3/18.4 ms; two-sided Mann-Whitney U-test: difference: -3.3, 95% CI [-4.0, -2.6], U = 1096, $p < 10^{-10}$).

We further tested the delay predictions by simultaneously recording AP responses in layer 4 and upper layer 6 of head-fixed, behaving rats. We implanted linear silicon probes with equally-spaced electrodes that spanned across the depth of wS1. This allowed to record the AP activity of several single units during awake conditions, and to determine the units' respective depth locations with ±50 µm precision. When animals explored their environment by rhythmically moving the principal whisker – all other whiskers were trimmed – sensory input was provided by whisker contact with a pole that was placed within range. AP responses in upper layer 6 preceded those in layer 4 of the same animal **(Fig. 3D)**. Across animals, the average AP onset in layer 4 was hence significantly delayed compared to layer 6 (Kolmogorov-Smirnov two-sample test: $D_{60,40} = 0.425$, $p < 0.01$), on average by 4 ms **(Fig. 3E)**. Our data reveal that inputs from primary thalamic axons can reliably drive fast APs in border stratum cells, providing the functional basis of a deep thalamorecipient pathway for sensory-evoked signal flow.

Manipulating border stratum cells affects broad tuning of cortical output

For the present conditions of single whisker deflections in anesthetized rats, AP responses of pyramidal tract neurons occurred near simultaneous with those in layer 4, and hence consistently later than in border stratum cells – approximately 3-4 ms (14.3/13.6/16.2 ms). One of the functions of the border stratum pathway could thus be that it is involved in driving cortical output patterns, whose onsets thereby

rival those in layer 4. In further supported of this hypothesis is the characteristic property of pyramidal tract neurons to respond to a broader range of stimuli compared to their thalamocortical input neurons [21]. In case of wS1, pyramidal tract neurons can respond similarly fast to stimulations of several whiskers [22], even if their dendrites are located hundreds of micrometers away from the terminal fields of those VPM axons that provide the respective thalamocortical input [23]. The extensive horizontally projecting axons in the deep layers, in combination with the earliest and reliable AP responses, hence render border stratum cells as ideal candidates that could contribute to the fast onsets and broadly tuned characteristics of cortical output patterns.

To test this hypothesis, we combined pharmacological injections of the $GABA_A$ agonist muscimol with cell-attached recordings in anesthetized rats **(Fig. 4A)**. Injection pipettes were positioned at the layer 5/6 border of wS1 by quantifying local field potentials (LFPs) at different cortical depths **(Fig. S4)**. The LFP recordings allowed mapping of the principal whisker that corresponded to the location of the injection site [24] – here referred to as the 'manipulated whisker'. Cell-attached recordings were performed in layer 5, approximately 1 millimeter away from the injection site. This distance assured that axons from border stratum cells, but not from other cell types that are affected by the pharmacology, overlap with the recording site **(Fig. 4B)**. Pyramidal tract neurons were identified as those that responded to deflections of several individual whiskers [22] – including the manipulated whisker **(Fig. 4C)**. After muscimol injections, fast responses evoked by the manipulated whisker were abolished in any of the recorded neurons **(Fig. 4D)**. In contrast, whiskers that were not somatotopically aligned with the injection site (e.g. the principal whisker at the recording site) maintained their ability to evoke reliable and fast AP responses **(Fig. 4E)**.

Border stratum cells provide an on-switch for cortical output

The pharmacological manipulations suggest that border stratum cells are necessary to drive the fast component of broadly tuned responses in pyramidal tract neurons. However, the high degree of recurrence in cortical networks, as well as non-linear mechanisms of synaptic and/or dendritic integration, pose a general challenge to infer causality between manipulations and the resultant alterations of neuronal AP responses. To address these issues, we developed a model that allows performing simulations that mimic the specific conditions of our *in vivo* pharmacology experiments at synaptic, cellular, and network levels, in the following referred to as *in silico* experiments. A link to download the model and simulation routines, and a detailed description and validation of all parameters, is provided in the **SI**. In brief, we embedded the morphology of an *in vivo* labeled pyramidal tract neuron into a previously reported anatomically realistic network model of rat wS1 [25]. The embedding provided structural constraints about which neurons, depending on their respective cell type and location within VPM and

wS1 (i.e., neurons represent *in vivo* labeled morphologies), can in principle form synaptic connections with the pyramidal tract neuron **(Fig. 5A)**, and where along its dendrites **(Fig. 5B)**. Combining the network model with cell type-specific AP measurements – acquired during conditions that were consistent with those of our pharmacology experiments [10, 23, 26] – provided functional constraints about which of the structurally possible connections can in principle provide input to the pyramidal tract neuron, depending on the identity of the stimulated whisker. We generated 1,800 of such structurally and functionally plausible synaptic input patterns for each of the 24 major facial whiskers**,** including those that correspond to the manipulated and principal whisker of our *in vivo* experiments **(Fig. 5C)**. Finally, we converted the pyramidal tract neuron into a multi-compartmental model **(Fig. S5)**, equipped with biophysical properties at the soma, dendrites, axon initial segment, and synapses that capture the characteristic intrinsic physiology of this cell type [27].

This multi-scale model allowed simulating how the dendrites of pyramidal tract neurons integrate and transform whisker-specific synaptic input patterns into AP output at the soma **(Movie S1)**. The simulations predicted responses that were indistinguishable from those recorded in pyramidal tract neurons *in vivo* **(Fig. 5D)**. In particular, AP probabilities and onsets in response to both, the principal and manipulated whisker, were in line with the respective *in vivo* data **(Fig. 5E)**. We hence performed pharmacology experiments *in silico*, at a level of spatial and cell type specificity that cannot be achieved *in vivo*. Deactivating only the border stratum cells within a volume that corresponds approximately to the spread of muscimol [7] abolished *in silico* responses to the manipulated whisker, but not to any other whisker **(Fig. 5F)**. Deactivating all neurons that may be affected by the muscimol, except for the border stratum cells, had in contrast no impact on the fast component of the simulated activity patterns. Deactivating all border stratum cells throughout wS1 predicted that pyramidal tract neurons lose their broadly tuned onset responses. However, the remaining direct input from the VPM is predicted to be still sufficient to evoke principal whisker responses, but with substantially reduced AP probabilities and later onsets. Our *in vivo* and *in silico* manipulations reveal that border stratum cells amplify the direct thalamocortical input of pyramidal tract neurons **(Fig. 5G)**, and relay sensory-evoked excitation from the local thalamorecipient volume to neurons across wS1, thereby driving the fast onsets of broadly tuned cortical output patterns.

We investigated which of the synaptic input parameters, or parameter combinations, of the multi-scale model could in general account for the fast onsets of sensory-evoked AP responses in pyramidal tract neurons. For each simulation trial we quantified the number of synapses that were active during the 25 ms following the stimulus onset, their respective path length distances to the soma, and times of activation at 1 ms resolution. A principal component analysis of these synaptic input statistics revealed that

simulation trials with and without fast AP responses formed systematically different distributions with respect to PC_1 **(Fig. 6A)**. 92% of the separation along the dimension of PC_1 could be attributed to a single quantity **(Fig. 6B)**, in the following referred to as synchronous proximal drive (SPD). SPD represents two effective parameters: the number and synchrony of active excitatory synapses that impinge onto the proximal dendrites (i.e., path length distance to the soma < 500 µm). SPD was an almost perfect predictor **(Fig. 6C)** for AP responses (i.e., area under the receiver operating curve (AUROC) equals 1) during simulations of passive whisker deflections (AUROC = 0.83±0.03). Simulations in which we systematically varied these two parameters hence provided general relationships between the number of proximal inputs that are active within a certain time window and the resultant probability of AP responses in pyramidal tract neurons **(Fig. 6D)**. Supporting the manipulation results, these simulations predicted that – for the present experimental conditions – only combined input from the VPM and border stratum cells would be sufficiently numerous and synchronous to drive the fast APs at response probabilities which match with those observed for PW, SW and MW deflections *in vivo*.

Discussion

We provide several lines of structural, functional, and computational evidence, which reveal the logic of bistratified thalamocortical input to rat wS1: preceding the vertical stream of sensory-evoked signal flow from layer 4 to layers 2/3, the strategically placed border stratum cells give rise to a second stream of excitation that spreads horizontally across layers 5/6. Parallel activation of layer 4 and a deep input stratum is likely to generalize to other sensory systems and species. For example in macaque V1, neurons – sometimes referred to as Meynert cells – have been described whose features are reminiscent of those that characterize the border stratum cells: they cluster around the layer 5/6 border and have extensive horizontal axons that span across the deep layers [4]. The function of Meynert cells remains unknown [28]. However, because of strong similarities in receptive field shapes between neurons in layers 4 and 6, it was suggested that these cells might be strategically placed to receive thalamocortical input from the deep layer terminal fields of lateral geniculate nucleus (LGN) axons [4]. It was even speculated that strong thalamocortical input to horizontally projecting neurons in the deep layers represents an organizational principle that is unique to primates, and which may underlie their superior cognitive capabilities [28]. However, bistratified LGN axons, as well as horizontally projecting thalamorecipient corticocortical neurons in the deep layers were also reported for V1 in cats [5, 29] and rodents [16].

We showed that the horizontal stream of excitation is necessary – and can even be sufficient – to drive fast sensory-evoked APs in pyramidal tract neurons. Bypassing the intracortical circuitry of the upper layers, the deep input stratum hence allows pyramidal tract neurons to integrate and transform sensory

inputs from differently tuned thalamocortical populations into cortical output, which can thereby contain the entire stimulus information that was simultaneously provided by the thalamus (e.g. multi-whisker [30] or binocular [31] stimuli in wS1 or V1). In addition to providing subcortical circuits with such an integrated efference copy of the sensory input [32], the fast activation of pyramidal tract neurons will also be critical for intracortical computations. Somatic APs back-propagate into the apical dendrites, triggering the activation of calcium channels [33] that widen the pyramidal tract neurons' time window for synaptic integration [34]. The fast back-propagating APs that are driven by the border stratum cells will therefore switch the dendrites of pyramidal tract neurons into an active state, which occurs near simultaneous with responses in layer 4 that are driven directly by the thalamus. The two input strata could hence complement each other, ensuring that pyramidal tract neurons are able to reliably transform inputs from recurrent intracortical circuits – e.g. those from layers 2/3 that are driven by layer 4 – into cortical output [35]. This theory is not only in line with the recent observation that sensory-evoked calcium transients in apical dendrites of pyramidal tract neurons correlate with perceptual thresholds during whisker-based behaviors [36]. It further provides a potential explanation for the origin of sustained AP responses in pyramidal tract neurons [14] that persist for the duration of the stimulus **(Fig. S6)**.

The deep input stratum will be involved in other functions, beyond regulating cortical output patterns. Axons of border stratum cells innervate all layers of wS1, but in particular layer 4. The fast and reliable activation of these neurons may therefore contribute to the substantial intracortical component of sensory-evoked post-synaptic potentials in the major thalamorecipient layer [37]. Moreover, at least a subset of the border stratum cells display long-range intrinsic axons that innervate higher-order cortices [38], a property that they share also with the Meynert cells [39]. Revealing how activity patterns can be coordinated across intracortical and subcortical circuits, the parallel strata principle provides insight that will be essential for understanding how the neocortex orchestrates sensory-guided behaviors.

Acknowledgements

We thank Bert Sakmann for discussions; Etay Hay and Idan Segev for providing biophysical models and optimization routines; Martin Schwarz for providing the AAV; Idan Segev, David Fitzpatrick and Kevan Martin for comments on the manuscript. Funding was provided by the European Research Council under the European Union's Horizon 2020 research and innovation program (No 633428), and in part by the German Federal Ministry of Education and Research Grants BMBF/FKZ 01GQ1002 and 01IS18052, and the Deutsche Forschungsgemeinschaft (SFB 1089). **We declare that we have no conflicting interests.**

Author contributions

M.O. conceived and designed the study. R.E. developed the model and performed simulations. R.N. performed cell-attached recordings, pharmacology experiments, and morphological reconstructions. D.U. developed analysis and data acquisition routines. A.B. performed simulations. J.G. performed virus injections and cell-attached recordings. S.D. performed extracellular recordings. C.K. performed cell-attached and extracellular recordings. All authors analyzed data. M.O. wrote the paper.

Figures and Figure Legends

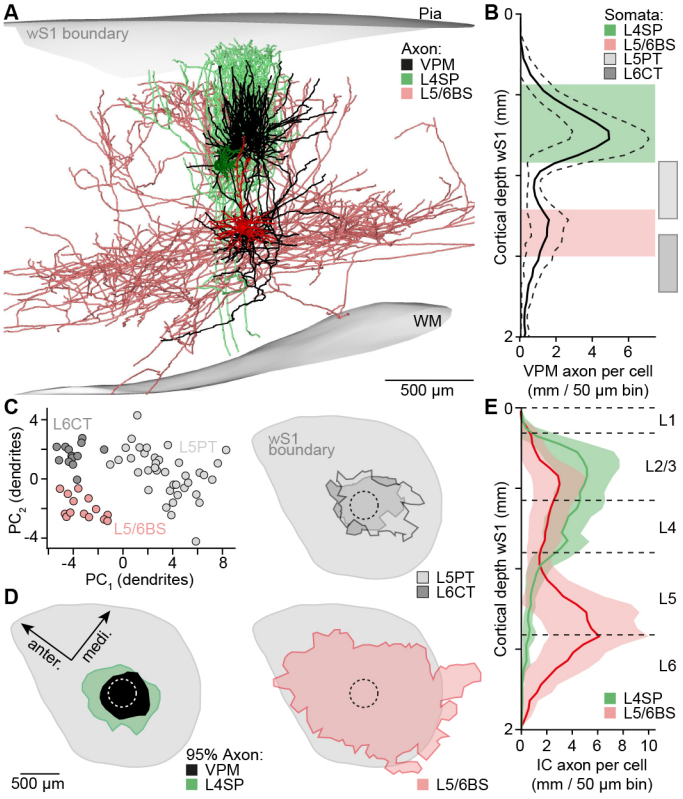

Figure 1: Structural basis of two thalamocortical input strata. A) Examples of *in vivo* labeled neurons in the whisker-related part of rat primary somatosensory cortex (wS1): layer 4 spiny neuron (L4SP), corticocortical neuron at the L5/6 border stratum (L5/6BS), and the intracortical (IC) part of the axon from a relay cell in the ventral posterior medial nucleus of the thalamus (VPM). **B)** Soma, dendrite and axon distributions of induvial neurons (n=191) were compared with 50 µm precision [9]. Somata of L4SP (n=37) and L5/6BS cells (n=14) cluster around the two innervation peaks of VPM axons (n=14, mean ± STD). Somata of L5/6BS cells intermingle with those of the subcortically projecting pyramidal tract (L5PT, n=38) and corticothalamic (L6CT, n=13) neurons. **C)** Principal components ($PC_{1/2}$) of dendritic features that discriminate between excitatory cell types in the deep layers [12, 13] (representing the cells in panel B). **D)**

Horizontal axon extent (95% iso-contours) of VPM (n=14), L4SP (n=14), L5PT (n=7), L6CT (n=11) and L5/6BS (n=9) neurons. Top views onto wS1. **E)** Vertical distributions of L4SP and L5/6BS axons (same cells as in panel D) vs. cytoarchitectonic layer borders [11].

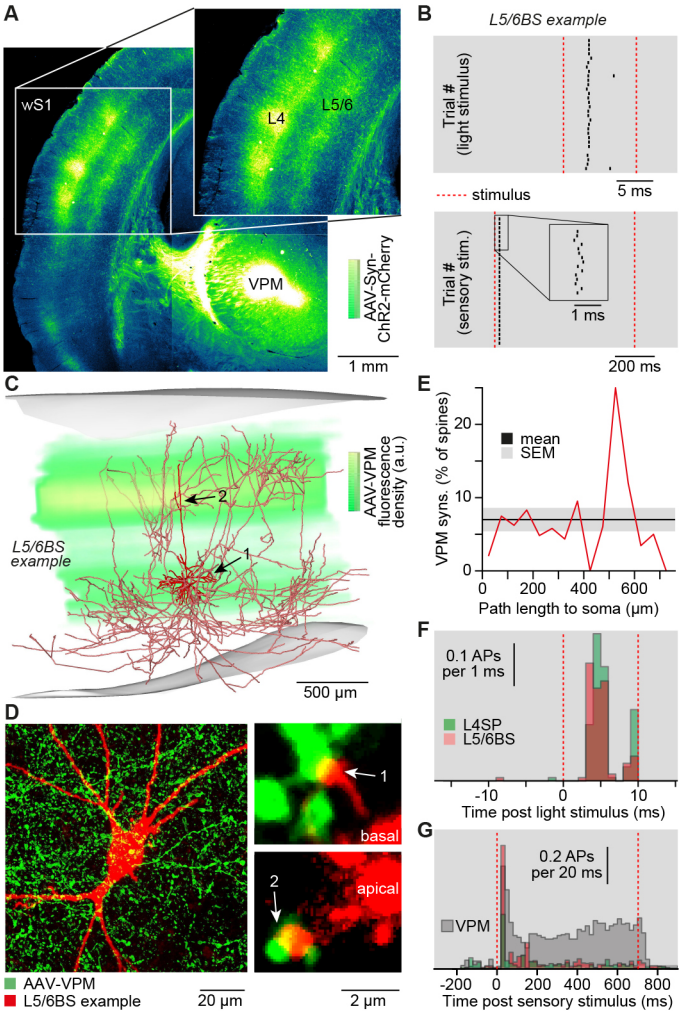

Figure 2: Synaptic basis of two thalamocortical input strata. A) Coronal brain section (50 µm) after injection of an adeno-associated virus (AAV) into the VPM, which expresses channel rhodopsin (ChR2) and a fluorescent marker (mCherry) in thalamocortical (TC) synapses. **B)** Example of cell-attached *in vivo* recording in wS1 of AAV-injected brain. Ticks represent APs in response to a 10 ms flash of green light onto the cortical surface (upper panel), and a 700 ms airpuff onto the whiskers (lower panel). **C)** Reconstruction of the L5/6BS cell shown in panel B, superimposed with quantification of AAV labeling. **D)** Confocal images of the L5/6BS cell shown in panel C. Putative TC synapses were identified as contacts between VPM boutons and dendritic spines. **E)** Fraction of spines (n=4789) along the dendrites of the L5/6BS cell shown in panel B-D that are contacted by VPM boutons. **F)** Post-stimulus-time-histograms (PSTHs) of light-evoked APs in L4SP and L5/6BS cells (mean ± STD of AP onset: 4.6±0.7

ms, n=4 vs. 4.4±0.8 ms, n=4). **G)** PSTHs of airpuff-evoked APs in L4SP, L5/6BS (same cells as in panel F) and VPM cells (n=7).

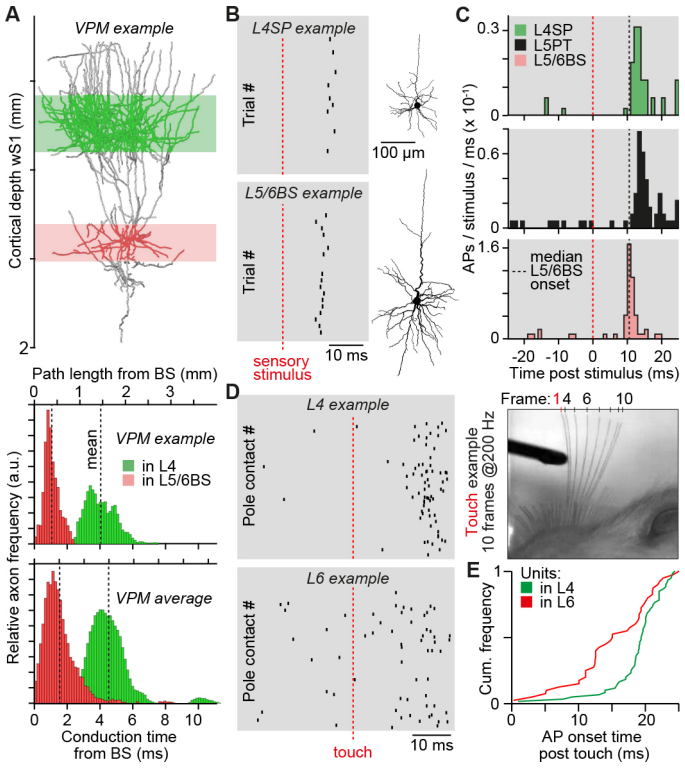

Figure 3: Functional basis of two thalamocortical input strata. A) Example of *in vivo* labeled VPM axon (upper panel), whose path length distribution was quantified with respect to the deepest location of the border stratum (L5/6BS), and multiplied with the IC conduction velocity (0.33 m/s [20]) of TC axons (center panel). Average conduction time of VPM axons (n=14) to the border stratum and layer 4 (lower panel). **B)** AP responses evoked by principal whisker (PW) deflections in exemplary L4SP and L5/6BS cells. **C)** PSTHs of PW-evoked APs in morphologically identified L4SP (n=8), L5PT (n=9) and L5/6BS (n=6) cells. **D)** Example of simultaneously recorded single units in layer 4 and upper layer 6 (~1.6 mm recording depth), which show reliable AP responses after PW contact with a pole during exploratory whisking (right panel: whisker positions after exemplary touch). **E)** Distribution of touch-evoked AP onsets across animals (n=3) in layer 4 and upper layer 6.

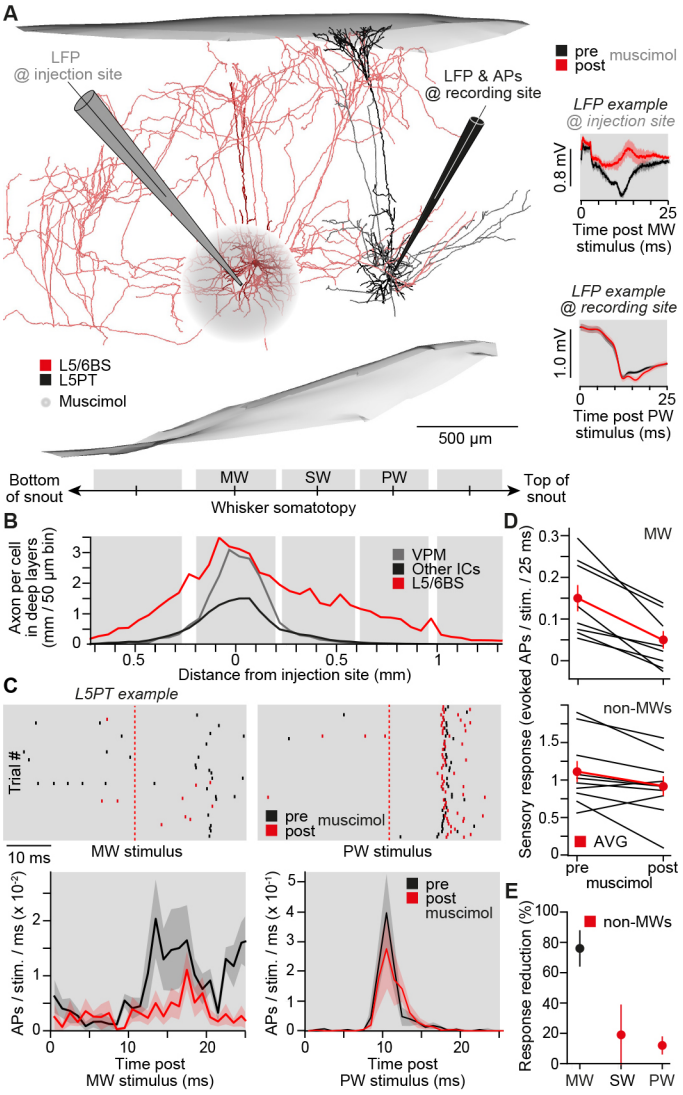

Figure 4: Onsets of broadly tuned cortical output patterns are driven by L5/6BS cells. A) The somatotopy of rat wS1 [9] in combination with whisker-evoked local field potential (LFP) measurements [24], allowed placing of muscimol injection and recording pipettes such that the respective PWs were separated by one whisker. Here the PW at the recording site is B2, the manipulated whisker (MW) is D2, and the separating whisker (SW) is C2. Left panel: L5/6BS and L5PT cells labeled in the same animal illustrate pharmacology experiments. Right panels: example LFPs before and after muscimol injections. **B)** Axonal extent in the deep layers from neurons located in the barrel column that represents the MW. **C)** Exemplary AP responses evoked by MW and PW deflections and PSTHs across cells (mean ± SEM; MW: n=8, PW: n=5). **D)** Response per cell to deflections of the MW (n=8, Wilcoxon rank-sum test: median = 0.095, 95% CI [0.05, 0.16], W=36, p=0.008) and non-MWs (PW & SW, n=5 & 5, Wilcoxon rank-sum test: median = 0.18, 95% CI [6×10^{-5}, 0.38], W=47.5, p=0.05) before and after muscimol injections. Mean ± SEM. **E)** Effect of muscimol on L5PT responses to deflections of the MW and non-MWs.

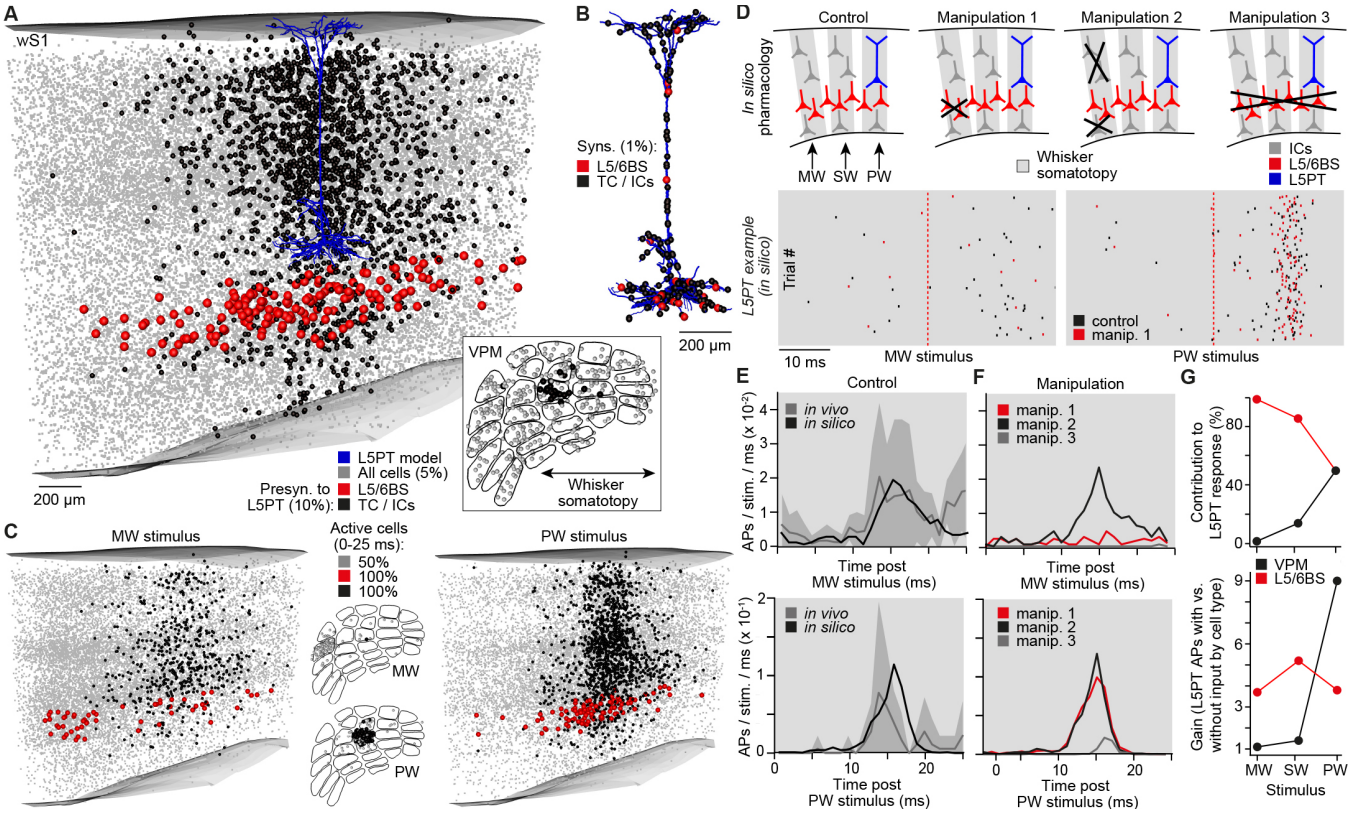

Figure 5: L5/6BS cells amplify and horizontally relay TC inputs to drive L5PT neurons. A) Example distribution of TC (i.e., inset represents model of VPM with barreloids) and IC neurons that provide synaptic input to a multi-compartmental L5PT model, embedded into an anatomically realistic model of rat wS1 [25]. **B)** Synapse locations along the dendrites of the L5PT model corresponding to the distribution of input neurons in panel A. **C)** Example distributions of VPM and IC neurons that provide synaptic input to the L5PT model during simulations of MW or PW deflections. **D)** Dendritic integration of such generated synaptic input patterns (i.e., for deflections of the MW, SW and PW, respectively) and transformation into somatic APs were simulated for four different (pharmacology) scenarios. Raster plots represent APs of the L5PT model for 200 of these input patterns, respectively. **E)** PSTHs predicted by the L5PT model (control scenario) and as measured *in vivo* for deflections of the PW (n=9) and MW (n=8). **F)** PSTHs predicted by the L5PT model for the three different manipulation scenarios. **G)** Relative fractions of VPM and L5/6BS synapses that provided input to the L5PT model during simulations of MW, SW and PW deflections (upper panel), and the respective amplifications of L5PT AP responses (lower panel).

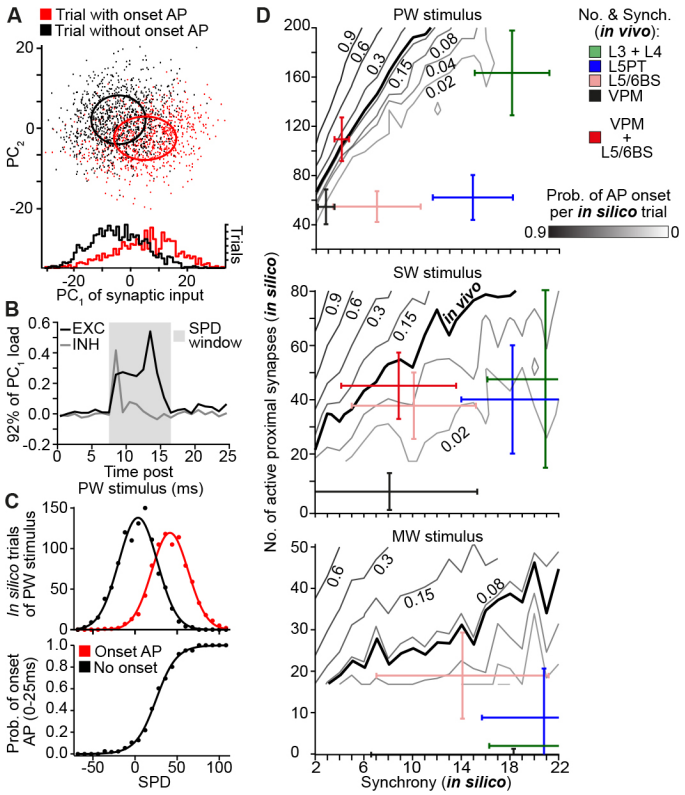

Figure 6: L5/6BS cells provide synchronous drive to proximal dendrites of L5PT neurons. **A.** PC analysis of spatiotemporal synaptic inputs that impinge onto the L5PT model during simulations of PW deflections. **B.** 92% of the separation between simulation trials with and without fast AP responses are reflected by PC_1, which represents the net excitatory input to proximal dendrites within a time window of 8-16 ms. These two parameters are combined into a single quantity: synchronous proximal drive (SPD). **C.** SPD is an almost perfect predictor for AP responses during simulations of the L5PT model. **D.** Probabilities of fast AP responses after simulations of PW, SW and MW deflections as predicted for different combinations of the number and synchrony of proximal inputs vs. cell type-specific data derived from empirical constraints of the model. Bold lines represent our *in vivo* measurements.

References

1. Bruno RM, Sakmann B. Cortex is driven by weak but synchronously active thalamocortical synapses. *Science* **312**, 1622-1627 (2006).
2. Harris KD, Shepherd GM. The neocortical circuit: themes and variations. *Nat Neurosci* **18**, 170-181 (2015).
3. Douglas RJ, Martin KA. Neuronal circuits of the neocortex. *Annu Rev Neurosci* **27**, 419-451 (2004).
4. Lund JS. Anatomical organization of macaque monkey striate visual cortex. *Annu Rev Neurosci* **11**, 253-288 (1988).
5. Antonini A, Stryker MP. Rapid remodeling of axonal arbors in the visual cortex. *Science* **260**, 1819-1821 (1993).

6. Oberlaender M, Ramirez A, Bruno RM. Sensory experience restructures thalamocortical axons during adulthood. *Neuron* **74**, 648-655 (2012).
7. Constantinople CM, Bruno RM. Deep cortical layers are activated directly by thalamus. *Science* **340**, 1591-1594 (2013).
8. Feldmeyer D*, et al.* Barrel cortex function. *Prog Neurobiol* **103**, 3-27 (2013).
9. Egger R, Narayanan RT, Helmstaedter M, de Kock CP, Oberlaender M. 3D reconstruction and standardization of the rat vibrissal cortex for precise registration of single neuron morphology. *PLoS Comput Biol* **8**, e1002837 (2012).
10. de Kock CP, Bruno RM, Spors H, Sakmann B. Layer- and cell-type-specific suprathreshold stimulus representation in rat primary somatosensory cortex. *J Physiol* **581**, 139-154 (2007).
11. Meyer HS, Egger R, Guest JM, Foerster R, Reissl S, Oberlaender M. Cellular organization of cortical barrel columns is whisker-specific. *Proc Natl Acad Sci U S A* **110**, 19113-19118 (2013).
12. Narayanan RT*, et al.* Beyond Columnar Organization: Cell Type- and Target Layer-Specific Principles of Horizontal Axon Projection Patterns in Rat Vibrissal Cortex. *Cereb Cortex* **25**, 4450-4468 (2015).
13. Oberlaender M*, et al.* Cell type-specific three-dimensional structure of thalamocortical circuits in a column of rat vibrissal cortex. *Cereb Cortex* **22**, 2375-2391 (2012).
14. Rojas-Piloni G, Guest JM, Egger R, Johnson AS, Sakmann B, Oberlaender M. Relationships between structure, in vivo function and long-range axonal target of cortical pyramidal tract neurons. *Nat Commun* **8**, 870 (2017).
15. Crandall SR, Patrick SL, Cruikshank SJ, Connors BW. Infrabarrels Are Layer 6 Circuit Modules in the Barrel Cortex that Link Long-Range Inputs and Outputs. *Cell Rep* **21**, 3065-3078 (2017).
16. Velez-Fort M*, et al.* The stimulus selectivity and connectivity of layer six principal cells reveals cortical microcircuits underlying visual processing. *Neuron* **83**, 1431-1443 (2014).
17. Schoonover CE*, et al.* Comparative strength and dendritic organization of thalamocortical and corticocortical synapses onto excitatory layer 4 neurons. *J Neurosci* **34**, 6746-6758 (2014).
18. Kumar P, Ohana O. Inter- and intralaminar subcircuits of excitatory and inhibitory neurons in layer 6a of the rat barrel cortex. *J Neurophysiol* **100**, 1909-1922 (2008).
19. O'Connor DH, Peron SP, Huber D, Svoboda K. Neural activity in barrel cortex underlying vibrissa-based object localization in mice. *Neuron* **67**, 1048-1061 (2010).
20. Salami M, Itami C, Tsumoto T, Kimura F. Change of conduction velocity by regional myelination yields constant latency irrespective of distance between thalamus and cortex. *Proc Natl Acad Sci U S A* **100**, 6174-6179 (2003).
21. Wright N, Fox K. Origins of cortical layer V surround receptive fields in the rat barrel cortex. *J Neurophysiol* **103**, 709-724 (2010).
22. Manns ID, Sakmann B, Brecht M. Sub- and suprathreshold receptive field properties of pyramidal neurones in layers 5A and 5B of rat somatosensory barrel cortex. *J Physiol* **556**, 601-622 (2004).
23. Brecht M, Sakmann B. Whisker maps of neuronal subclasses of the rat ventral posterior medial thalamus, identified by whole-cell voltage recording and morphological reconstruction. *J Physiol* **538**, 495-515 (2002).
24. Lee JH, Shin HS, Lee KH, Chung S. LFP-guided targeting of a cortical barrel column for in vivo two-photon calcium imaging. *Sci Rep* **5**, 15905 (2015).
25. Egger R, Dercksen VJ, Udvary D, Hege HC, Oberlaender M. Generation of dense statistical connectomes from sparse morphological data. *Front Neuroanat* **8**, 129 (2014).
26. Bruno RM, Simons DJ. Feedforward mechanisms of excitatory and inhibitory cortical receptive fields. *J Neurosci* **22**, 10966-10975 (2002).
27. Hay E, Hill S, Schurmann F, Markram H, Segev I. Models of neocortical layer 5b pyramidal cells capturing a wide range of dendritic and perisomatic active properties. *PLoS Comput Biol* **7**, e1002107 (2011).
28. Briggs F. Organizing principles of cortical layer 6. *Front Neural Circuits* **4**, 3 (2010).

29. Karube F, Sari K, Kisvarday ZF. Axon topography of layer 6 spiny cells to orientation map in the primary visual cortex of the cat (area 18). *Brain Struct Funct* **222**, 1401-1426 (2017).
30. Ramirez A, Pnevmatikakis EA, Merel J, Paninski L, Miller KD, Bruno RM. Spatiotemporal receptive fields of barrel cortex revealed by reverse correlation of synaptic input. *Nat Neurosci* **17**, 866-875 (2014).
31. Li H, Fukuda M, Tanifuji M, Rockland KS. Intrinsic collaterals of layer 6 Meynert cells and functional columns in primate V1. *Neuroscience* **120**, 1061-1069 (2003).
32. Sherman SM. Thalamus plays a central role in ongoing cortical functioning. *Nat Neurosci* **19**, 533-541 (2016).
33. Markram H, Helm PJ, Sakmann B. Dendritic calcium transients evoked by single back-propagating action potentials in rat neocortical pyramidal neurons. *J Physiol* **485 (Pt 1)**, 1-20 (1995).
34. Larkum ME, Zhu JJ, Sakmann B. A new cellular mechanism for coupling inputs arriving at different cortical layers. *Nature* **398**, 338-341 (1999).
35. Hay E, Segev I. Dendritic Excitability and Gain Control in Recurrent Cortical Microcircuits. *Cereb Cortex* **25**, 3561-3571 (2015).
36. Takahashi N, Oertner TG, Hegemann P, Larkum ME. Active cortical dendrites modulate perception. *Science* **354**, 1587-1590 (2016).
37. Cohen-Kashi Malina K, Mohar B, Rappaport AN, Lampl I. Local and thalamic origins of correlated ongoing and sensory-evoked cortical activities. *Nat Commun* **7**, 12740 (2016).
38. Zhang ZW, Deschenes M. Intracortical axonal projections of lamina VI cells of the primary somatosensory cortex in the rat: a single-cell labeling study. *J Neurosci* **17**, 6365-6379 (1997).
39. Fries W, Keizer K, Kuypers HG. Large layer VI cells in macaque striate cortex (Meynert cells) project to both superior colliculus and prestriate visual area V5. *Exp Brain Res* **58**, 613-616 (1985).

Methods and Supplement only

40. Narayanan RT, Mohan H, Broersen R, de Haan R, Pieneman AW, de Kock CP. Juxtasomal biocytin labeling to study the structure-function relationship of individual cortical neurons. *J Vis Exp*, e51359 (2014).
41. Boudewijns ZS*, et al.* Layer-specific high-frequency action potential spiking in the prefrontal cortex of awake rats. *Front Cell Neurosci* **7**, 99 (2013).
42. Clack NG*, et al.* Automated tracking of whiskers in videos of head fixed rodents. *PLoS Comput Biol* **8**, e1002591 (2012).
43. Siegle JH, Lopez AC, Patel YA, Abramov K, Ohayon S, Voigts J. Open Ephys: an open-source, plugin-based platform for multichannel electrophysiology. *J Neural Eng* **14**, 045003 (2017).
44. Rossant C*, et al.* Spike sorting for large, dense electrode arrays. *Nat Neurosci* **19**, 634-641 (2016).
45. Bartho P, Hirase H, Monconduit L, Zugaro M, Harris KD, Buzsaki G. Characterization of neocortical principal cells and interneurons by network interactions and extracellular features. *J Neurophysiol* **92**, 600-608 (2004).
46. Wong-Riley M. Changes in the visual system of monocularly sutured or enucleated cats demonstrable with cytochrome oxidase histochemistry. *Brain Res* **171**, 11-28 (1979).
47. Horikawa K, Armstrong WE. A versatile means of intracellular labeling: injection of biocytin and its detection with avidin conjugates. *J Neurosci Methods* **25**, 1-11 (1988).
48. Oberlaender M, Bruno RM, Sakmann B, Broser PJ. Transmitted light brightfield mosaic microscopy for three-dimensional tracing of single neuron morphology. *J Biomed Opt* **12**, 064029 (2007).
49. Dercksen VJ, Hege HC, Oberlaender M. The Filament Editor: an interactive software environment for visualization, proof-editing and analysis of 3D neuron morphology. *Neuroinformatics* **12**, 325-339 (2014).

50. Mainen ZF, Carnevale NT, Zador AM, Claiborne BJ, Brown TH. Electrotonic architecture of hippocampal CA1 pyramidal neurons based on three-dimensional reconstructions. *J Neurophysiol* **76**, 1904-1923 (1996).
51. Druckmann S, Banitt Y, Gidon A, Schurmann F, Markram H, Segev I. A novel multiple objective optimization framework for constraining conductance-based neuron models by experimental data. *Front Neurosci* **1**, 7-18 (2007).
52. Hines ML, Carnevale NT. The NEURON simulation environment. *Neural Comput* **9**, 1179-1209 (1997).
53. Arzt M, Sakmann B, Meyer HS. Anatomical Correlates of Local, Translaminar, and Transcolumnar Inhibition by Layer 6 GABAergic Interneurons in Somatosensory Cortex. *Cereb Cortex*, 1-12 (2017).
54. Helmstaedter M, Sakmann B, Feldmeyer D. L2/3 interneuron groups defined by multiparameter analysis of axonal projection, dendritic geometry, and electrical excitability. *Cereb Cortex* **19**, 951-962 (2009).
55. Koelbl C, Helmstaedter M, Lubke J, Feldmeyer D. A barrel-related interneuron in layer 4 of rat somatosensory cortex with a high intrabarrel connectivity. *Cereb Cortex* **25**, 713-725 (2015).
56. Egger R, Schmitt AC, Wallace DJ, Sakmann B, Oberlaender M, Kerr JN. Robustness of sensory-evoked excitation is increased by inhibitory inputs to distal apical tuft dendrites. *Proc Natl Acad Sci U S A* **112**, 14072-14077 (2015).
57. Feldmeyer D, Lubke J, Silver RA, Sakmann B. Synaptic connections between layer 4 spiny neurone-layer 2/3 pyramidal cell pairs in juvenile rat barrel cortex: physiology and anatomy of interlaminar signalling within a cortical column. *J Physiol* **538**, 803-822 (2002).
58. Wozny C, Williams SR. Specificity of synaptic connectivity between layer 1 inhibitory interneurons and layer 2/3 pyramidal neurons in the rat neocortex. *Cereb Cortex* **21**, 1818-1826 (2011).
59. Jahr CE, Stevens CF. A quantitative description of NMDA receptor-channel kinetic behavior. *J Neurosci* **10**, 1830-1837 (1990).
60. Larkum ME, Nevian T, Sandler M, Polsky A, Schiller J. Synaptic integration in tuft dendrites of layer 5 pyramidal neurons: a new unifying principle. *Science* **325**, 756-760 (2009).
61. Schnepel P, Kumar A, Zohar M, Aertsen A, Boucsein C. Physiology and Impact of Horizontal Connections in Rat Neocortex. *Cereb Cortex* **25**, 3818-3835 (2015).
62. Gupta A, Wang Y, Markram H. Organizing principles for a diversity of GABAergic interneurons and synapses in the neocortex. *Science* **287**, 273-278 (2000).
63. Petersen CC, Hahn TT, Mehta M, Grinvald A, Sakmann B. Interaction of sensory responses with spontaneous depolarization in layer 2/3 barrel cortex. *Proc Natl Acad Sci U S A* **100**, 13638-13643 (2003).
64. Reyes-Puerta V, Sun JJ, Kim S, Kilb W, Luhmann HJ. Laminar and Columnar Structure of Sensory-Evoked Multineuronal Spike Sequences in Adult Rat Barrel Cortex In Vivo. *Cereb Cortex* **25**, 2001-2021 (2015).
65. Lefort S, Tomm C, Floyd Sarria JC, Petersen CC. The excitatory neuronal network of the C2 barrel column in mouse primary somatosensory cortex. *Neuron* **61**, 301-316 (2009).
66. Thomson AM, West DC, Wang Y, Bannister AP. Synaptic connections and small circuits involving excitatory and inhibitory neurons in layers 2-5 of adult rat and cat neocortex: triple intracellular recordings and biocytin labelling in vitro. *Cereb Cortex* **12**, 936-953 (2002).
67. Brown SP, Hestrin S. Intracortical circuits of pyramidal neurons reflect their long-range axonal targets. *Nature* **457**, 1133-1136 (2009).
68. Perin R, Berger TK, Markram H. A synaptic organizing principle for cortical neuronal groups. *Proc Natl Acad Sci U S A* **108**, 5419-5424 (2011).
69. Song S, Sjostrom PJ, Reigl M, Nelson S, Chklovskii DB. Highly nonrandom features of synaptic connectivity in local cortical circuits. *PLoS Biol* **3**, e68 (2005).
70. Thomson AM, West DC, Hahn J, Deuchars J. Single axon IPSPs elicited in pyramidal cells by three classes of interneurones in slices of rat neocortex. *J Physiol* **496 (Pt 1)**, 81-102 (1996).

Methods

Animal preparation: All experiments were carried out after evaluation by the local German authorities, in accordance with the animal welfare guidelines of the Max Planck Society, or with the Dutch law after evaluation by a local ethical committee at the VU University Amsterdam, The Netherlands.

Virus injection: Male Wistar rats aged 22-25 days (P22-25, m, Charles River) were anesthetized with isoflurane supplemented by rimadyl (Caprofen, 5mg/ kg) as analgesia, then placed into a stereotaxic frame (Kopf Instruments, model 1900), and provided with a continuous flow of isoflurane/O_2 gas. Body temperature was maintained at 37°C by a heating pad. A small craniotomy was made above the left hemisphere 2.85 mm posterior to bregma and 3.2 mm lateral from the midline. The head of the rat was leveled with a precision of 1 µm in both the medial-lateral and anterior-posterior planes using an eLeVeLeR electronic leveling device (Sigmann Electronics, Hüffenhardt, Germany) mounted to an adapter of the stereotaxic frame. An injecting pipette containing an adeno-associated virus (AAV) was lowered into the VPM thalamus (5.05 mm from the pia). The virus – rAAV2/1-CAG-hChR2(H134R)-Syn-mCherry (titer: 1x1012 gc ml^{-1}) – was provided by Martin Schwarz (University of Bonn, Germany). 50-70 nL of the virus were injected using a 30cc syringe coupled to a calibrated glass injection capillary.

Cell-attached recording/labeling in virus injected animals: After a 16-21 day incubation period, AAV injected rats were anesthetized with urethane (1.8 g/kg body weight) by intraperitoneal injection. The depth of anesthesia was assessed by monitoring pinch withdrawal, eyelid reflexes, and vibrissae movements. Body temperature was maintained at 37.5 ± 0.5 °C by a heating pad. Cell-attached recording and labeling was performed as described in detail previously [40]. Briefly, APs were recorded using an extracellular loose patch amplifier (ELC-01X, npi electronic GmbH), and digitized using a CED power1401 data acquisition board (CED, Cambridge Electronic Design, Cambridge, UK). APs were recorded before and during 20-30 trials of caudal multi-whisker deflections by a 700 ms airpuff (10 PSI), delivered through a 1 mm plastic tube from a distance of 8-10 cm from the whisker pad [14]. Stimulation was repeated at constant intervals (0.3 Hz). Optical stimulation of ChR2-expressing thalamocortical terminals was provided by a 200 µm diameter optical fiber (ThorLabs #RJPSF2) coupled to a 470 nm wavelength LED (ThorLabs M470F3), resulting in an output power of 1 mW. The fiber was positioned approximately 2 mm above the cortical surface, resulting in a 1-2 mm disc of light above wS1. APs were recorded during 20-30 trials of 10 ms light pulses, at an inter-stimulus interval of 2.5 s. Following the electrophysiological measurements, neurons were filled with biocytin. Filling sessions were repeated several times. After 1-2 hours for tracer diffusion, animals were transcardially perfused with 0.9% saline followed by 4%

583 paraformaldehyde (PFA). Brains were removed and post-fixed with 4% PFA for 24 hours, transferred to
584 0.05 M phosphate buffer (PB) and stored at 4°C.
585
586 **Pharmacological manipulation:** Wistar rats (P28-P35, m, Charles River) were anesthetized with
587 urethane (1.6-1.7 g/kg body weight) by intraperitoneal injection. As described above, the depth of
588 anesthesia was monitored, and the animal's body temperature was maintained. An 'L' shaped craniotomy
589 centered on the coordinate of the barrel column representing the D2 whisker (2.5 mm posterior and 5.5
590 mm lateral to the bregma) was made without cutting the dura, and extended along the rostro-medial (i.e.,
591 along the E-row) and caudal axes (i.e., arc 2) for ~1-2 mm, respectively. Locations for muscimol injections
592 and recordings were determined with long-tapered 'search pipettes' (tip diameter <3 µm and insertion
593 diameter <50µm). The search pipette was inserted rostral to wS1 and lowered parallel to the midline
594 while measuring LFPs at different cortical depths, and in response to deflections of different individual
595 whiskers using a piezoelectric bimorph [24]. Recordings were made using an Axoclamp 2B amplifier (Axon
596 instruments, Union City, CA, USA), low pass filtered (300 Hz), and digitized using a CED power1401 data
597 acquisition board (CED, Cambridge Electronic Design, Cambridge, UK). Using the LFP data, we identified
598 the depth of the L5/6 border and the principal whisker (e.g. E2), and marked this location on the dura with
599 a surgical pen. Repeating the LFP-guided whisker mapping with a second search pipette that was
600 inserted approximately parallel to the vertical axis of wS1, we identified layer 5 of the hence appropriate
601 recording site (i.e., C2 if the injection pipette was located at E2). This location was also marked on the
602 dura. Pipettes for muscimol injections were prepared with a tip diameter of 8-12 µm. The taper diameter
603 at the insertion point into the brain was ~125-150 µm. The tip of the pipette was filled with normal rat
604 ringer (NRR) to avoid muscimol spill upon pipette insertion. The rest of the pipette was filled with 10 mM
605 muscimol supplemented with 2% biocytin. The injection pipette was positioned at the previously
606 determined location, the dura was cut open (~500 µm), and the injection pipette was inserted with positive
607 pressure of 5-10 mbar. Allowing the tissue to adjust for 10-15 minutes, we inserted a recording pipette
608 (i.e., 1 µm tip diameter, filled with NRR supplemented with 2% biocytin) at the second previously
609 determined location. Both locations were confirmed by measuring whisker-evoked LFPs. Pyramidal tract
610 neurons were identified as follows [10, 13, 22]: (1) recording depth between 1000-1600 µm; (2) ongoing AP
611 rates between ~1-5 Hz; (3) reliable and fast APs (i.e., between 10-20 ms) in response to principal whisker
612 deflections; (4) reliable and fast APs after deflection of the manipulated whisker. We identified eight
613 neurons that matched these criteria (recording / injection location: 1x B1/D1, 4x C1/E1, 3x C2/E2).
614 Whisker deflections of the PW (e.g. C2), one SW (e.g. D2) and the MW (e.g. E2) were performed (i.e.,
615 50 trials of 200 ms ramp-and-hold stimulus with an amplitude of ~5°, 2 s inter-stimulus interval), and APs
616 were recorded, while simultaneously measuring the LFP via the injection pipette. Following these

617 measurements (i.e., control data), muscimol was injected by slowly increasing the pressure onto the
618 injection pipette (80-300 mbar), while monitoring the LFP in response to MW deflections. Once MW-
619 evoked LFPs were abolished, and the AP activity remained unaffected, the measurements of whisker-
620 evoked responses were repeated (i.e., at least 50 trials of PW, SW and MW deflections, respectively).
621
622 **Extracellular recordings:** Wistar rats (P33-P70, m) were anesthetized using 1.6 % isoflurane in 0.4 l/h
623 O_2 + 0.7 l/h NO_2, supplemented by rimadyl (Caprofen, 5mg/ kg) as analgesia. A craniotomy of 0.5 mm x
624 0.5 mm was made above wS1 on the left hemisphere, and a head post for fixation was implanted on the
625 skull. After recovery from surgery, rats were head-fixed two times per day for 2-3 days. Rats quickly
626 adjusted to the head-fixation, allowing stable recording conditions without the need of body restraint. Rats
627 were anaesthetized with isoflurane (1.25% in 0.4 l/h O_2 + 0.7 l/h NO_2), and a 32-channel linear silicon
628 probe (E32+R-50-S1-L10(NT), Atlas Neuroengineering, Belgium) was inserted into wS1 for extracellular
629 multi-unit recordings. Prior to recordings, silicon probes were labeled with DiI (Thermo Fisher Scientific,
630 Waltham, MA, USA). The probe was connected to a unity-gain headstage (Neuralynx, USA), in series
631 with the Open Ephys data acquisition board equipped with a RHD2132 digital interface chip (Intan
632 Technologies, Los Angeles, CA, USA). Using the LFP strategy described above, the PW at the recording
633 site was identified, all other whiskers were trimmed to 5 mm, and the anesthesia was terminated.
634 Recordings were performed once the animals were fully awake (~25 minutes after the anesthesia was
635 terminated [41]). Rats were not trained to perform tactile behavior, and behavior was not rewarded. Sensory
636 input resulted from whisker touch with a pole that was placed within range during periods of exploratory
637 whisker self-motion. The touch onset was determined by high-speed videography at 200 frames/s
638 (MotionScope M3 camera, IDT Europe, Belgium). Whisker angle was tracked offline [42], and episodes of
639 whisker movements were classified by thresholding average power in whisker angle versus time (1-20
640 Hz bandpass) using the Matlab spectrogram function. Touch events were detected manually in each
641 frame. Signals were acquired at a sampling rate of 30 kHz/channel using Open Ephys GUI [43]. To identify
642 single units, the data were high-pass filtered, and automatically sorted into clusters using Klustakwik [44].
643 The clusters were manually post-processed, and only stable and well-isolated single units were
644 considered for analysis. The average waveforms of all well-isolated single units were used to sub-classify
645 units [45] as regular spiking vs. fast spiking units (FSUs). FSUs (AP peak-to-trough time <0.5 ms and AP
646 half-peak time <0.25 ms) were excluded from the analyses. After recordings, rats were anaesthetized
647 with urethane (>2.0 g/kg) and perfused with 0.9% NaCl followed by 4% paraformaldehyde (PFA).
648
649 **Histology:** For morphological reconstructions, 100 µm thick vibratome sections were cut tangentially to
650 wS1 (45° angle) ranging from the pial surface to the white matter (WM). Sections were processed for

cytochrome-C oxidase staining to visualize barrel contours in layer 4 [46]. All sections were treated with avidin-biotin (ABC) solution, and subsequently neurons were identified using the chromogen 3,3′-diaminobenzidine tetrahydrochloride (DAB) [47]. All sections were mounted on glass slides, embedded with Mowiol, and enclosed with a cover slip. In experiments where AAV injections were combined with biocytin filling, cortex was cut into 45-48 consecutive 50 µm thick tangential sections. Sections were treated with Streptavidin Alexa-488 conjugate (5mg/ml Molecular Probes #S11223) to stain biocytin labeled morphologies [14]. To enhance the virus labeling, sections were immunolabeled with anti-mCherry antibody. Sections were permeabilized and blocked in 0.5% Triton x-100 (TX) (Sigma Aldrich #9002-93-1) in 100 mM PB containing 4% normal goat serum (NGS) (Jackson ImmunoResearch Laboratories #005-000-121) for 2 hours at room temperature. The primary antibody was diluted 1:500 (Rabbit anti-mCherry, Invitrogen #PA5-34974) in PB containing 1% NGS for 24 hours at 4°C. The secondary antibody was diluted (1:500 goat anti-Rabbit IgG Alexa-647 H+L Invitrogen #A21245) and was incubated for 2-3 hours at room temperature in PB containing 3% NGS and 0.3% TX. All sections were mounted on glass slides, embedded with SlowFade Gold (Invitrogen #S36936) and enclosed with a cover slip. For extracellular recording experiments, brains were post-fixed in 4% PFA, and tangential vibratome sections (100 µm) were cut and stained for cytochrome-C. An X-Cite 120 Q light-source (Excelitas Technologies Corp., Waltham, MA, USA) was used to visualize the DiI electrode tract, and only electrode tracks within the barrel column that represents the PW were selected for analyses. The histology allowed assigning the recording depth to each electrode (i.e., and hence to each unit) with approximately 100 µm precision.

Morphological reconstruction: Neuronal structures were extracted from image stacks using a previously reported automated tracing software [48]. 3D image stacks of up to 5 mm × 5 mm × 0.1 mm were acquired using an automated brightfield microscope system (BX-51, Olympus, Japan) at a resolution of 0.092 × 0.092 × 0.5 µm per voxel (100× magnification, NA 1.4). For reconstruction of fluorescently labeled neurons, images were acquired using a confocal laser scanning system (Leica Application Suite Advanced Fluorescence SP5; Leica Microsystems). 3D image stacks of up to 2.5 mm × 2.5 mm × 0.05 mm were acquired at a resolution of 0.092 × 0.092 × 0.5 µm per voxel (63× magnification, NA 1.3). Manual proof-editing of individual sections, and automated alignment across sections were performed using custom-designed software [49]. Pia, barrel and WM outlines were manually drawn on low resolution images (4×). Using these anatomical reference structures, all reconstructed dendrite and axon morphologies were registered to the D2 barrel column of a standardized 3D reference frame of rat wS1 [9]. The shortest distance from the pial surface to the soma, and 20 morphological features that have previously been shown to separate between excitatory cell types in rat wS1 [9] were calculated for each reconstructed and registered dendrite morphology. For identification of putative thalamocortical

685 synapses, biocytin labeled morphologies and AAV labeled VPM terminals were imaged simultaneously
686 using the confocal laser scanning system as described above: biocytin Alexa-488 (excited at 488 nm,
687 emission detection range 495-550 nm), AAV Alexa-647 (excited at 633 nm, emission detection range
688 650-785 nm). These dual-channel 3D image stacks were loaded into Amira visualization software (FEI).
689 All reconstructed dendrites were manually inspected, and landmarks were placed onto each spine head.
690 If a spine head was overlapping with a VPM bouton, an additional landmark was placed to mark a putative
691 synapse. The shortest distance of each landmark to the dendrite reconstruction was determined, and the
692 path length distance was calculated from that location along the reconstructed L5/6BS cell to the soma.
693
694 **Cell type-specific analysis:** In total, n=177 *in vivo* labeled morphologies of excitatory neurons in wS1
695 (i.e., from urethane anesthetized Wistar rats; P25-P45, m/f, Charles River) were used in this study to
696 determine cell type-specific whisker receptive fields (wRFs), and to provide structural/functional
697 constrains for simulation experiments. All morphologies [12, 14] – except for five L5/6BS and one L5PT
698 neurons – and classification approaches [12, 13], as well as the corresponding whisker-evoked physiology
699 data [10, 13] have been reported previously, but in different context. Analysis of wRFs for objectively
700 classified morphological cell types were not performed for any of the previously reported neurons. Here,
701 each neuron was objectively assigned to one of the 10 major excitatory cell types of the neocortex [2, 12]
702 based on the 21 soma-dendritic features described above: three types of pyramids in layers 2-4 (L2PY,
703 L3PY, L4PY), spiny-stellates (L4ss) and star-pyramids in layer 4 (L4sp), slender-tufted intratelencephalic
704 (L5IT) and thick-tufted pyramidal tract neurons in layer 5 (L5PTs), polymorphic corticocortical (L6CC) and
705 corticothalamic neurons in layer 6 (L6CT), and the L5/6 border stratum cells (L5/6BS). In the present
706 study, we grouped L4ss and L4sp as layer 4 spiny neurons (L4SP). The physiology data (i.e., AP
707 responses to passive deflections of the principal and its eight adjacent whiskers [10]) were grouped by the
708 hence determined morphological cell types, resulting cell type-specific wRFs.
709
710 **Multi-compartmental model:** We generated a biophysically-detailed multi-compartmental neuron
711 model, which captures the stereotypic morphological and intrinsic physiological properties of L5PTs. The
712 L5PT model is based on the 3D soma-dendrite reconstruction of a L5PT neuron, whose morphological
713 and topological features – which allow discriminating L5PTs from other excitatory cell types in the deep
714 layers (see above) – represent approximately the respective averages across a population of 37 L5PTs
715 [12, 14] that were labeled *in vivo* via cell-attached recordings in layer 5 of rat wS1. A simplified axon
716 morphology was attached to the reconstructed soma based on [50]. The axon consisted of an axon hillock
717 with a diameter tapering from 3.5 µm to 1 µm over a length of 10 µm, an axon initial segment (AIS) of 10
718 µm length and 1 µm diameter, and 1 mm of myelinated axon (diameter of 1 µm). The diameter of the

719 reconstruction of the apical trunk and oblique dendrites was scaled by a factor of 2.5 to allow for
720 backpropagation of action potentials (bAP), and bAP-triggered calcium spike (BAC) firing to occur (i.e.,
721 after scaling the diameter of the apical trunk was 4.5 µm at the soma, and 1.5 µm at the main bifurcation
722 located at a distance of ~900 µm from the soma). Spatial discretization of the dendrite morphology (i.e.,
723 compartmentalization) was performed by computing the electrotonic length constant of each dendrite
724 branch at a frequency of 100 Hz and setting the length of individual compartments in this branch to 10%
725 of this length constant. The length of axonal compartments was set to 10 µm. After spatial discretization,
726 the L5PT morphology consisted of 1033 compartments with an average length of ~15 µm, but no longer
727 than 42 µm. The resultant L5PT model was then combined with previously reported biophysical models
728 of a variety of Hodgkin-Huxley (HH)-type ion channels **(Table S1)** that are expressed at different densities
729 within the soma, basal and/or apical dendrites, and axon initial segment [27]. Using an evolutionary multi-
730 objective optimization algorithm [51], we tuned the parameters of the biophysical models until numerical
731 simulations of the L5PT model (using NEURON 7.2 [52]) reproduced current injection-evoked somatic
732 and/or dendritic sub- and suprathreshold responses that are characteristic for L5PTs, as measured
733 previously via whole-cell recordings in acute brain slices of rat wS1 *in vitro* [27]. Fixed membrane
734 parameters were the axial resistance (100 Ωcm in all compartments), the membrane capacitance (1
735 $\mu F/cm^2$ at the soma and axon, 2 $\mu F/cm^2$ in the apical and basal dendrites to account for increased surface
736 area due to spines, and 0.04 $\mu F/cm^2$ along the myelinated part of the model axon), and the passive
737 membrane conductance along the myelinated part of the axon (g_{pas} = 0.4 $pS/\mu m^2$, i.e., equivalent to a
738 specific membrane resistance of 25,000 Ωcm^2). The reversal potential of the passive membrane
739 conductance was set to -90 mV. Conductance densities of the non-specific cation current I_h were fixed at
740 0.8 $pS/\mu m^2$ in the soma and axon, and 2 $pS/\mu m^2$ in the basal dendrites. In the apical dendrite, the
741 conductance density of I_h increased exponentially with the distance to the soma. The biophysical model
742 parameters to be optimized were the peak conductance per unit membrane area for various voltage-
743 dependent ion channels, and the parameters of a phenomenological model of the calcium dynamics in
744 different parts of the morphology (i.e., axon, soma, basal and apical dendrites; **Table S1**). The targets of
745 the optimization were different features of the membrane potential in response to two stimuli, as
746 measured previously [27]: (1) a brief current injection into the soma should trigger an AP at the soma and
747 a bAP, and (2) a brief current injection into the soma, followed by current injection into a Ca^{2+} channel
748 dense region around the first bifurcation point of the apical tuft, should trigger somatic bursts (i.e., BAC
749 firing). The specific features, as listed in **Table S2**, were combined into five objectives, which were then
750 optimized simultaneously by using the evolutionary algorithm [51]. A set of 1,000 models was generated
751 with parameters drawn randomly from a physiologically plausible range. In every iteration, each model
752 was then evaluated by simulating the response to the two stimuli, calculating the features and determining

753 the error by calculating the difference between each simulated and measured feature in units of standard
754 deviations of the experimental feature [27]. After each model had been evaluated, a new set of 1,000
755 models was generated from the previous set by stochastically transferring parameter values from "good"
756 models (i.e., lower errors) to "worse" models (i.e., higher errors). Additionally, parameter values of all
757 models were updated stochastically to avoid converging to local minima. This procedure was repeated
758 500 times. From the final iteration, the set of biophysical models used here was selected based on three
759 criteria: (1) it had the lowest sum across all objective errors, (2) similar deviations in all objective errors
760 (i.e., models where only a subset of objectives matched the experimental data were not considered), and
761 (3) it supported regular spiking of increasing frequencies in response to sustained current injections of
762 increasing amplitude.
763
764 **Connectivity model:** The structurally plausible constraints for the numbers and dendritic distributions of
765 cell type-specific synaptic input patterns that impinge onto the L5PT model are based on an anatomically
766 realistic network model of rat wS1, as described in detail previously [25]. Briefly, we generated a 3D model
767 of the average geometry of rat wS1 (i.e., 3D location, orientation and diameter of all barrel columns; 3D
768 pial and white matter (WM) surfaces), and determined the variability (~50 µm) of these anatomical
769 landmarks across twelve animals [9]. Next, we measured the number and 3D distribution of all excitatory
770 and inhibitory neuron somata in rat wS1 (~530,000 neurons) and the ventral posterior medial nucleus
771 (VPM) of the thalamus (~6,000 neurons) in four different animals [11], and generated an average excitatory
772 and inhibitory 3D neuron somata distribution at a resolution of 50x50x50 μm^3, reflecting the variability of
773 the cortex geometry across animals. We then registered a sample of 177 excitatory intracortical (IC)
774 neuron morphologies (i.e., grouped into ten cell types (see above) [10, 12], 14 excitatory thalamocortical
775 (TC) axon morphologies labeled in VPM *in vivo* [6], and the soma-dendrites of 213 inhibitory neuron (IN)
776 morphologies (203 labeled in L2-6 *in vitro* [53, 54, 55], 10 labeled in L1 *in vivo* [56]) to the geometric model of
777 wS1. Combining these data by using a previously reported network building approach [25], we generated
778 a structurally dense model of wS1, which comprised soma, dendrite and axon morphologies that
779 represent all of the excitatory (here: 462,402) and inhibitory neurons (here: 67,535) that are located in rat
780 wS1, as well as axon morphologies that represent the IC part of all VPM neurons (here: 6,225). To
781 estimate synaptic connectivity within this structurally dense wS1 model, we calculated the overlap at 50
782 μm^3 resolution between the putative postsynaptic target structures (PSTs; i.e., soma/dendrite surface for
783 inhibitory connections; dendritic spines for excitatory connections) and putative presynaptic sites (i.e.,
784 axonal boutons) for all pairs of neurons, and normalized this quantity by the respective total amount of
785 locally available PSTs (i.e., total somatic/dendritic surface and number of spines within each 50 µm
786 voxel). Neglecting wiring specificity at subcellular scales [25], we converted these overlap measurements

into connection probabilities, which predict the respective distributions of the numbers and most likely dendritic locations of synaptic contacts. To compare the predicted connection probabilities between excitatory IC cell types and L5PTs with previously reported paired-recording results that were obtained from acute brain slices *in vitro*, we cropped out ten 300 µm wide thalamocortical/semi-coronal slices from the network model, which comprised at least half of the C2 barrel column volume. Connection probabilities that were predicted for truncated morphologies in slices are denoted by asterisks in **Table S3**. To compare the predicted connection probabilities between TC neurons and L5PTs with previously reported paired-recording results that were obtained *in vivo*, we used L5PTs whose somata were closest to the C2 barrel column (i.e., including septal neurons) and TC neurons located in the C2 VPM-barreloid of the uncropped network model. To compare the predicted connection probabilities between INs and L5PTs with previously reported paired-recording results we grouped all excitatory neurons in layer 5 (i.e., L5PTs and L5ITs) whose somata were closest to the C2 barrel column (i.e., including septal neurons) and INs whose axons remained largely confined to layer 5. Finally, we embedded the L5PT model into the network model of wS1 by using a previously reported registration approach [9]. Here, we placed the L5PT model at nine different locations within the barrel column representing the C2 whisker (i.e., approximately in the center of wS1), while preserving its (*in vivo*) soma depth location. For each of the nine locations (i.e., one in the column center, and eight at equally spaced angular intervals with a distance of ~100 µm to the column center) we used the connectivity mapping procedures as described above to estimate the numbers and dendritic locations of cell type-specific synaptic inputs that impinge onto the dendrites of the L5PT model. Specifically, by sampling from the overlap distributions 50 times, calculating the mean of the number of synaptic inputs from each cell type, and choosing the sample that was closest to this mean, we estimated that the L5PT model receives a total of 24,161 ± 785 synaptic inputs. Of those, ~90% are predicted to originate from excitatory IC and TC neurons, which corresponds to an average density of 1.4 glutamatergic and 0.14 GABAergic synapses per µm dendrite, respectively (i.e., 148 ± 18 GABAergic synapses are located on the soma).

Synapse models: Conductance-based synapses were modeled with a double-exponential time course. Excitatory synapses contained both AMPA receptors (AMPARs) and NMDARs. Inhibitory synapses contained $GABA_A$Rs. The reversal potential of AMPARs and NMDARs was set to 0 mV, that of $GABA_A$Rs to -75 mV. Rise and decay time constants of AMPARs were set to 0.1 ms and 2 ms, respectively [57]; those of NMDARs to 2 ms and 26 ms, respectively [57]; and those of $GABA_A$Rs to 1 ms and 20 ms, respectively [58]. The Mg-block of NMDARs was modeled by multiplying the conductance value with an additional voltage-dependent factor $1/(1 + \eta \cdot \exp(-\gamma \cdot V))$ [59], where $\eta = 0.25$, $\gamma = 0.08/\text{mV}$, and V is the membrane potential in mV [60]. The peak conductance at excitatory synapses from different presynaptic cell types was

821 determined by assigning the same peak conductance to all synapses of the same cell type, activating all
822 connections of the same cell type (i.e., all synapses originating from the same presynaptic neurons) one
823 at a time, and comparing parameters of the resulting unitary postsynaptic potential (uPSP) amplitude
824 distribution (mean, median and maximum) for a fixed peak conductance with experimental
825 measurements *in vitro* (input from L2-6 [61]) or *in vivo* (TC input [7]). The peak conductance for synaptic
826 inputs from each cell type was systematically varied until the squared differences between the parameters
827 of the *in silico* and *in vitro*/*in vivo* uPSP amplitude distributions were minimized **(Table S4)**. The peak
828 conductance at inhibitory synapses was fixed at 1 nS [35]. Release probability at excitatory and inhibitory
829 synapses was fixed at 0.6 and 0.25, respectively [35, 62].
830
831 **Synaptic input patterns:** Synaptic input patterns to the L5PT model were estimated as follows: All
832 presynaptic neurons determined during the network-embedding procedure were converted into point
833 neurons that could emit APs. During periods of ongoing activity, APs in presynaptic neurons were
834 modeled as Poisson trains with cell type-specific mean firing rates as measured *in vivo* [13]. The mean
835 firing rate of INs was set to 7 Hz [35] (except for L1 INs [56]). Each AP in a presynaptic neuron is registered
836 at all synapses between the presynaptic neuron and the L5PT model without delay and may cause a
837 conductance change, depending on the release probability of the synapse. After a stimulus (i.e.,
838 deflection of the PW, SW or MW), each presynaptic neuron can emit additional spikes. The location of
839 the deflected whisker in the wRF of the presynaptic neuron is determined based on the barrel column
840 where the soma of the presynaptic neuron is located in (i.e., a convolution operation), and the
841 corresponding whisker-specific post-stimulus time histogram (PSTH) is used to stochastically generate
842 additional sensory-evoked APs. Whisker-specific PSTHs of excitatory cell types were generated based
843 on *in vivo* wRF measurements (**Fig. S3)**. The amplitude of the PSTH of excitatory IC cell types is further
844 scaled by a factor of 0.4571 to reflect lower response probabilities of cortical neurons in the up-state [63].
845 The whisker-specific PSTHs of TC neurons in VPM were constructed based on previously published *in*
846 *vivo* measurements, where single- and multi-whisker responsive neurons were described for the same
847 experimental conditions used in this study [23]. Single- and multi-whisker responsive VPM neurons were
848 grouped into a single TC PSTH. The whisker-specific PSTHs of INs in wS1 were constructed based on
849 previously published *in vivo* measurements, which were acquired under the same experimental
850 conditions that were used here [26, 64], and which can be summarized as follows: (1) the onset times of
851 whisker-evoked APs in INs across all layers should be similar to those of the excitatory cell types; (2) in
852 case of PW touch, AP onset times in INs should precede those of the excitatory IC, but not TC cell types;
853 (3) INs have broad wRFs. To capture these empirical constraints, the PW/SW-evoked PSTHs of INs were
854 set to the respective maximum values across all excitatory cell types in each 1 ms time bin; the resultant

PW-evoked PSTH was shifted by -1 ms (but no spiking before TC neurons; i.e., > 8 ms); and the ratio between the integrals of the PW- and SW-evoked PSTHs during 0-50 ms was set to a fixed ratio of 2:1. These constraints leave one free parameter for constructing the PSTHs of INs: the total number of PW-evoked APs during 0-50 ms post stimulus. We simulated the response of the L5PT model after PW deflections while systematically varying this parameter, and computed the resulting number of APs during 0-25 ms, until the L5PT model exhibited simulation trials with and without AP responses as measured *in vivo*. This yielded a value for INs of 1.0 APs per PW deflection per 50 ms. *In silico* pharmacology experiments were performed by removing all synaptic inputs from specific presynaptic populations from the model as shown in **Fig. 5D**.

Simulations: We generated 200 samples of structurally- and functionally-plausible cellular stimulus representations for each of the nine L5PT model locations (i.e., 1,800 samples per whisker), and for each simulated whisker deflection in the control condition (i.e., the complete network model), and for three different *in silico* pharmacology experiments. Since the L5PT model was located in the C2 column, simulated C2 deflections were assigned as PW deflections, those of the eight adjacent whiskers as SW deflections, and simulated E2 deflections as MW deflections. The three different *in silico* pharmacology conditions were as follows: (1) synapses from border stratum (L5/6BS) cells whose somata were located within the E2 column or the surrounding septum were removed from the L5PT model; (2) synapses from neurons of all excitatory cell types whose somata where located within the E2 column, except for L5/6BS cells, were removed; (3) synapses from all L5/6BS cells throughout wS1 were removed. All combinations of L5PT model location, identity of the deflected whisker, and pharmacology condition resulted in 72,000 spatiotemporal synaptic input patterns, which we associate with different trials. For each trial, we numerically simulated the integration of the respective conductance changes within all dendritic compartments (and the soma and axon) of the HH-type L5PT model. Each simulation trial consisted of 245 ms ongoing activity, followed by 50 ms of sensory-evoked activity. The first 100 ms and the last 25 ms of simulated activity were discarded. AP times were determined from zero-crossings of the simulated membrane potential at the soma. For each of the simulation trials (control condition) we created a 100-dimensional vector, which quantified the spatiotemporal features of the respective synaptic input patterns that impinge onto the L5PT model. Entries of the vector represented all active synapses during the period of 0-25 ms post stimulus, their respective path length distances to the soma, times of activation with 1 ms resolution, and whether the synapses originated from excitatory or inhibitory neurons. The input vectors were sorted into two groups, representing simulations in which onset APs (i.e., during the period of 8-25 ms post stimulus) did or did not occur. A principal component analysis (PCA) of these spatiotemporal input vectors revealed that trials with vs. without onset APs formed overlapping, but

systematically different distributions. PC_1 discriminated between these distributions. 92% of PC_1 could be accounted for by the difference between excitatory and inhibitory inputs that are active during a period of 8-16 ms post stimulus, and that are located within less than 500 µm path length distance to the soma (here referred to as proximal inputs). We defined a single quantity that represents PC_1 – synchronous proximal drive (SPD) – i.e., it reflects the net input (i.e., number of active excitatory minus active inhibitory synapses) along the proximal dendritic compartments of the L5PT model (i.e., path length distance <500 µm) within 8-16 ms. We then calculated the probability of observing a whisker-evoked AP response in the L5PT model as a function of SPD, and fitted a sigmoidal curve to this distribution. The inverse width (or slope) of the fitted sigmoidal curve can be interpreted as a measure for the predictive power of SPD for AP responses. We systematically varied the end time point of the integration time window to determine the SPD window with highest predictive power, which matched closely with the SPD window determined for PW deflections by the PCA. These SPD windows were then used to compute the AUROC values for PW and SW deflections reported in the main text. Breaking down SPD into its two parameter, (1) the number of active excitatory synapses along the proximal dendrites, and (2) their respective synchrony (i.e., time window in which they are active), we performed additional simulations of the L5PT model. To do so, the structurally and functionally constrained PW/SW-evoked spatiotemporal synaptic input patterns were replaced as follows. All other model parameters (i.e., biophysical and synapse models), as well as synaptic input patterns preceding the stimulus remained unchanged. First, the distribution of stimulus evoked synaptic inputs along the dendrites of L5PT model was determined by calculating the average distribution of active synapses during 50 ms following PW and SW simulation trials (i.e., from the structurally and functional constrained trails). Second, the resultant 3D distributions of active excitatory and inhibitory synapses were converted into distance-dependent probability distributions (i.e., 1D) with 50 µm (i.e., path length) resolution. Third, the subcellular distributions, temporal activation patterns and numbers of active synapses (i.e., excitatory/inhibitory during periods of ongoing activity; inhibitory during periods of whisker-evoked activity) were then determined by calculating the respective averages across PW and SW simulation trials (i.e., from the structurally and functional constrained trails), respectively. Fourth, the temporal distribution of active excitatory synapses was modeled as a log-normal distribution [10] with a fixed offset of 8 ms post-stimulus (i.e., corresponding to the onset latency of VPM input) and a fixed peak time of 9 ms post-stimulus. Fifth, the only remaining parameter was the median timing of the log-normal distribution. Varying this parameter in 1 ms steps resulted in excitatory synaptic input distributions that ranged from highly synchronous (2 ms; i.e., median timing at 10 ms post stimulus) toward asynchronous (i.e., median timing much later than 10 ms post stimulus). Sixth, at the same time, the total number of active excitatory synaptic inputs was systematically varied. Seventh, for each combination of the number and synchrony of stimulus evoked excitatory inputs, 200 samples of

spatiotemporal synaptic input patterns were generated and simulated as described above. Then, the probability of an onset AP (i.e., between 8-16 ms) was calculated for each combination of the number and synchrony of stimulus evoked excitatory inputs. Iso-AP probability contour plots were calculated by arranging all synaptic input number and synchrony combinations in a 2D grid, and linear interpolation between the grid points. The corresponding *in vivo* data of cell type-specific numbers and synchronies of active proximal inputs were derived from the structural and functional simulation constraints of PW, SW and MW deflections (i.e., representing our *in vivo* measurements **(Fig. S3)** and reconstructions of the network model **(Fig. S5)**).

Statistical analysis: All data are reported as mean ± standard deviation unless mentioned otherwise. Normality was not assumed when performing statistical testing. All tests were performed using the R software package (version 3.4.3) and the scipy python package (version 1.0.1).

Data availability: All relevant data are available from the authors. The model and simulation routines, including a detailed documentation of all parameters and the analysis routines can be obtained from ModelDB (http://senselab.med.yale.edu/ModelDB/; accession number: 239145; password: Horizontal).

Supplementary Materials for:

Thalamus drives two complementary input strata of the neocortex in parallel

R. Egger[1]†‡, R.T. Narayanan[1]†, D. Udvary[1], A. Bast[1], J.M. Guest[1], S. Das[2], C.P.J. de Kock[2], M. Oberlaender[1]*

[1]Max Planck Group: In Silico Brain Sciences, Center of Advanced European Studies and Research, Bonn, Germany; [2]Department of Integrative Neurophysiology, Center for Neurogenomics and Cognitive Research, VU Amsterdam, The Netherlands.

*Correspondence to: marcel.oberlaender@caesar.de;

†These authors contributed equally.

‡Current address: Neuroscience Institute, NYU School of Medicine, New York, USA.

The Supplement includes: Figures S1 to S6

Tables S1 to S4

Movie S1

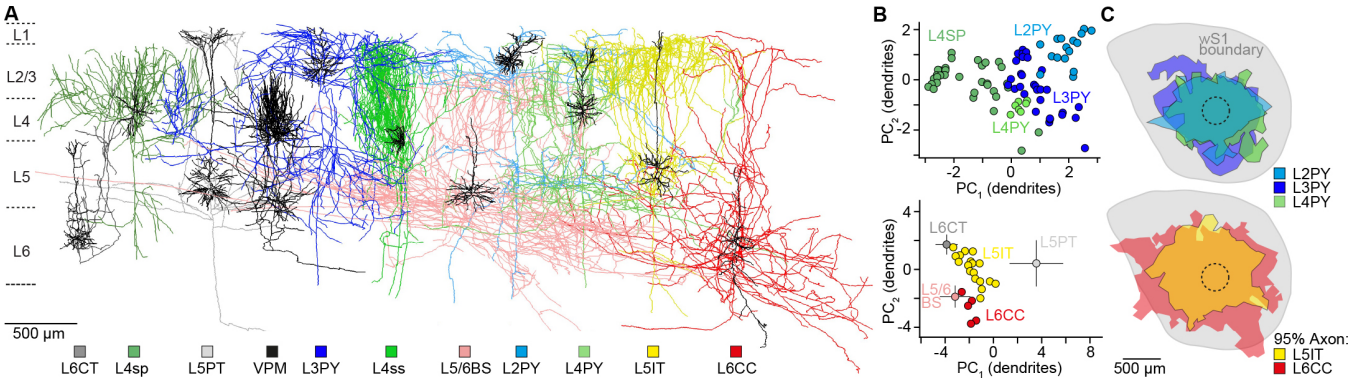

Figure S1: Cell type-specific structural constrains for *in silico* experiments. A) Gallery of exemplary *in vivo* labeled neuron morphologies for each of the 10 major excitatory cell types of the neocortex, whose soma, dendrite and axon distributions (ICs, n=177) were compared with the laminar distribution of thalamocortical axons from the ventral posterior medial nucleus (VPM, n=14). Neurons were classified as reported previously [12] into pyramidal neurons in layer 2 (L2PY, n=16), layer 3 (L3PY, n=30) and layer 4 (L4PY, n=7), spiny stellates (L4ss, n=22) and star-pyramids in layer 4 (L4sp, n=15), slender-tufted intratelencephalic (L5IT, n=18) and thick-tufted pyramidal tract neurons in layer 5 (L5PT, n=37), corticothalamic (L6CT, n=13) and polymorphic corticocortical neurons in layer 6 (L6CC, n=5), and corticocortical neurons at the layer 5/6 border (L5/6BS, n= 14). L4ss and L4sp neurons were grouped as layer 4 spiny neurons (L4SP). **B)** Principal components ($PC_{1/2}$) of dendritic features that discriminate between excitatory cell types in the upper and deep layers, respectively. The means and STDs of L5/6BS, L5PT and L6CT neurons from **Fig. 1C** are shown for comparison. **D)** Horizontal axon extent of L2PY (n=9), L3PY (n=15), L4PY (n=4), L5IT (n=5) and L6CC (n=4) neurons.

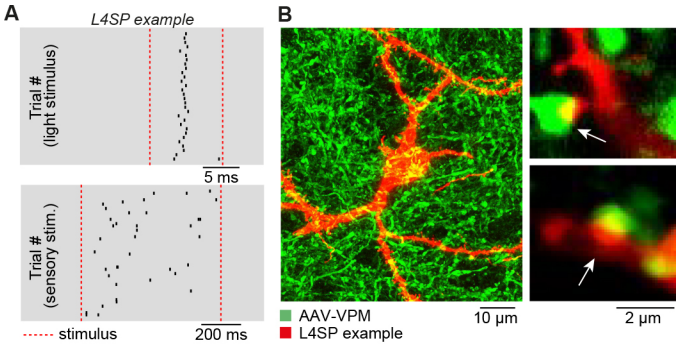

Figure S2: Thalamocortical input to L4SP cells. A) Example of cell-attached *in vivo* recording in layer 4 of wS1 of AAV-injected brain. Ticks represent APs in response to a 10 ms flash of green light onto the cortical surface (top), and a 700 ms airpuff onto the whiskers (bottom). **B)** Confocal images of the neuron shown in panel A. The neuron was morphologically identified as L4SP. Putative thalamocortical synapses were identified as contacts between VPM boutons and dendritic spines.

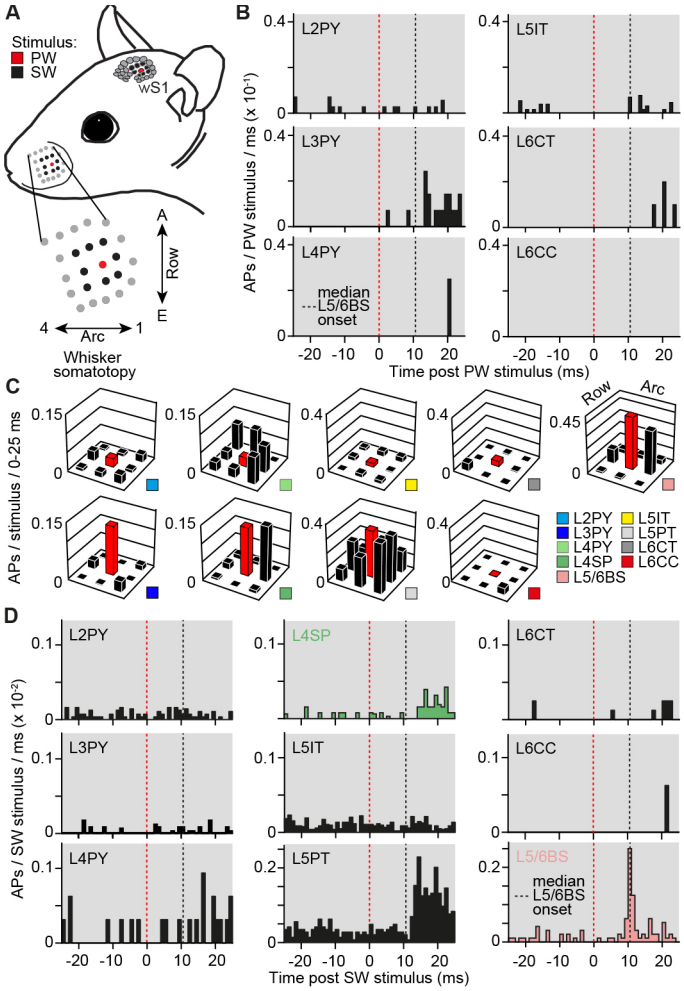

Figure S3: Cell type-specific functional constrains for *in silico* experiments. A) Illustration of cell type-specific mapping of whisker receptive fields (wRFs) as reported previously [10] (i.e., under conditions that were consistent with those of the pharmacological manipulations). Action potentials (APs) were recorded in responses to deflections of the principal whisker (PW), and of the eight whiskers that are adjacent to the PW (here referred to as SWs). **B)** PSTHs of PW-evoked APs for morphologically classified L2PY (n=7), L3PY (n=7), L4PY (n=2), L5IT (n=13), L6CT (n=5) and L6CC (n=1) neurons, analogous to those shown in **Fig. 3C** for L4SP, L5PT and L5/6BS neurons. **C)** Cell type-specific wRFs representing the cells in panels B and D. **D)** PSTHs of SW-evoked APs for all cell types (i.e., averaged across the adjacent whiskers), representing the cells shown in panels B and C, and **Fig. 3C**.

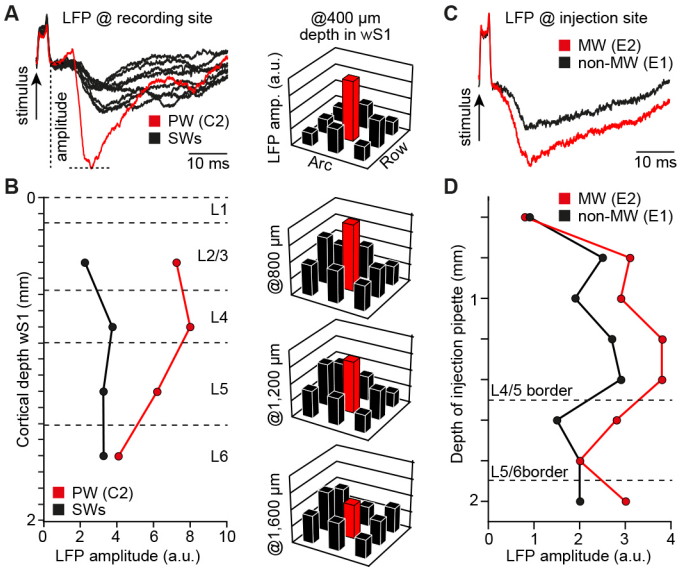

Figure S4: LFP guided *in vivo* pharmacology. A) Left panel: LFP recordings via search pipette at 400 µm depth in wS1. LFP amplitudes in response to deflections of the PW and its eight SWs were quantified. Right panel: LFP wRF reveals the PW at the recording site [24] (here: C2). **B.** LFP wRF measurements were repeated at different cortical depths of wS1. Using the depth of layer borders [11], the characteristic laminar profiles of LFP responses to PW (and SW) stimuli were used to identify the border between layer 4 and 5 (i.e., ~100 µm below the LFP maximum). The target location at the L5/6 border was hence approximately 400-500 µm below the LFP maximum. **C-D)**. Example experiment that illustrates how the LFP depth profile was used to locate the L5/6 border of the barrel column representing the MW whisker (i.e., E2). The muscimol injection pipette was inserted rostral to wS1 at an angle that was approximately parallel to the midline (i.e., oblique to the vertical axis of wS1). E2 was identified as the MW based on the larger LFP amplitudes across the cortical depth when compared to those evoked by SW stimuli (shown here: E1). The target location (i.e., L5/6 border) was then determined by identifying the depth of maximal LFP amplitude and adding 500 µm (i.e., here injection at ~1850 µm depth).

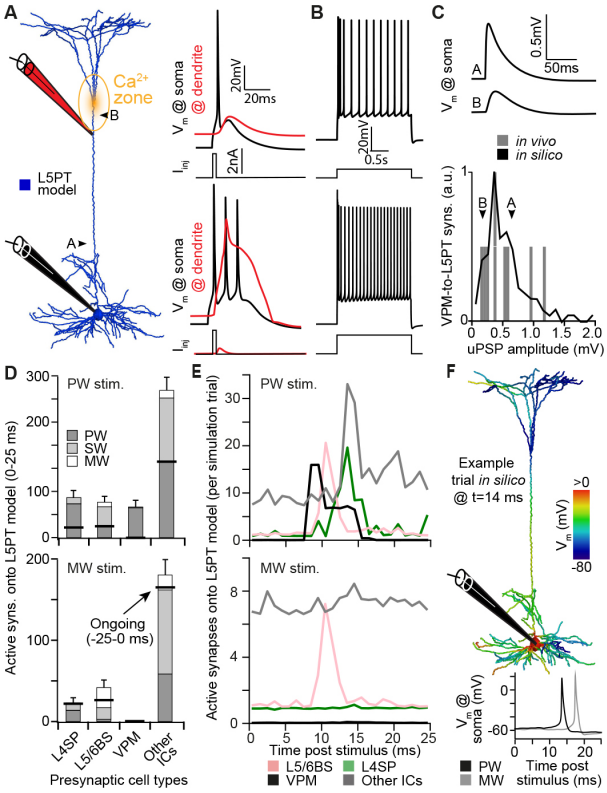

Figure S5: Intrinsic physiological and synaptic constrains for *in silico* experiments. A) Left panel: L5PT neuron model, consisting of 1033 dendritic compartments with previously reported biophysical models [27]. The parameters of the biophysical models were tuned until numerical simulations reproduced current injection-evoked responses that are characteristic for L5PT neurons (right panels): (1) a brief current injection into the soma triggers an AP that back-propagates into the apical dendrite (bAP), and (2) a brief current injection into the soma, followed by current injection into a Ca^{2+} channel dense region around the first bifurcation point of the apical tuft, triggers somatic bursts (i.e., BAC firing). **B)** The model supported regular AP firing of increasing frequencies in response to sustained current injections of increasing amplitude. **C)** The peak conductance at excitatory synapses from different presynaptic cell types was optimized to match empirical unitary post-synaptic-potential (uPSP) amplitude distributions (here exemplified for VPM-to-L5PT synapses [7]). **D)** The neuron model was embedded into an anatomically realistic network model of rat wS1 and VPM. Based on cell type-specific axo-dendritic overlap (using the morphologies shown in **Fig. 1** and **Fig. S1**) and wRF measurements (**Fig 3** and **Fig. S3**), plausible synaptic input patterns to the L5PT neuron model were generate for deflections of different whiskers. The number (mean ± STD across simulation trials) of active synapses that impinge onto the neuron model during the first 25 ms after simulations of PW and MW deflections are shown. Horizontal black lines denote the number of active synapses that each cell type contributes also to 25 ms of ongoing activity (i.e., before the stimulus). Different grey shadings denote the location of the presynaptic neurons

(i.e., somatotopically aligned with the PW, SW or MW). **E)** The number (mean across simulation trials) of active synapses that impinge onto the neuron model during each millisecond of the first 25 ms after simulations of PW and MW deflections, respectively. Other ICs represent inputs from all excitatory intracortical cell types, except for the border stratum cells. **F)** Exemplary simulation trial for synaptic input patterns as shown in panels D and E, which are integrated by the dendrites of the L5PT neuron model (upper panel) and transformed into somatic APs (lower panel).

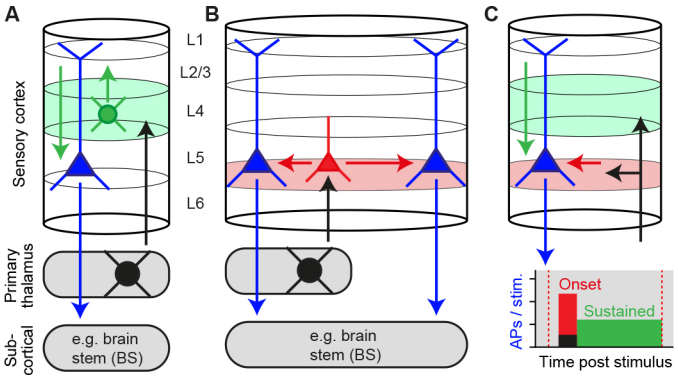

Figure S6: Suggested concept of primary sensory cortex. Sensory-evoked thalamocortical input is relayed in parallel by two orthogonally organized thalamorecipient populations which give rise to complementary canonical pathways: vertical to layers 2/3 by L4SP neurons **(A)**, and horizontally to layers 5/6 by L5/6BS cells **(B)**. The deep thalamorecipient pathway activates pyramidal tract neurons, whereas signal flow in the upper layers terminates in layer 5. The complementary pathway theory hence provides a potential explanation for sustained AP responses in pyramidal tract neurons that persist for the duration of the stimulus. We showed that one way to drive cortical output is by providing sufficiently strong and synchronous synaptic input to the proximal dendrites. However, synchrony decreases during recurrent excitation within local and long-range cortical circuits. Moreover, a substantial fraction of these recurrent and top-down inputs will impinge onto distal dendrites (e.g. within L1). It is hence unlikely that sustained responses in pyramidal tract neurons originate from the same mechanism as the onset responses (see also [14]). We thus hypothesize that the L5/6BS cell-driven onset responses are required to switch the apical dendrites into an active state, which allows pyramidal tract neurons to transform temporally less synchronous and spatially more distributed synaptic inputs (e.g. from layers 2/3) into sustained patterns.

Parameter	Soma	AIS / Myelin	Apical dendrite	Basal dendrites
C_m (µF/cm^2)	1.0	1.0 / 0.04	2.0	2.0
r_a (Ωcm)	100	100 / 100	100	100
g_{pas} ($1/r_m$)	0.326	0.256 / 0.4	0.882	0.631
Na_t	24300	880 / –	252	–
Na_p	49.9	14.6 / –	–	–
K_t	471	841 / –	–	–
K_p	0	7730 / –	–	–
SKv3.1	9830	9580 / –	112	–
SK E2	492	0.577 / –	34	–
Ca_{LVA}	46.2	85.8 / –	1040*	–
Ca_{HVA}	6.42	6.92 / –	45.2*	–
τ_{Ca} (ms)	770	507 / –	133	–
γ_{Ca} (1)	0.000616	0.0175 / –	0.0005	–
I_m	–	– / –	1.79	–
I_h	0.8	0.8 / –	$A+B\cdot\exp(C\cdot d/d_{max})$ **	2

Table S1. Biophysical parameters of the L5PT model. These parameters were obtained using the multi-objective optimization algorithm described previously [27, 51]. Units for different ion channel densities are pS/µm^2. τ_{Ca} (ms) is the time constant of the calcium buffering model, and γ_{Ca} is a dimensionless parameter describing the calcium buffer affinity. g_{pas}: passive membrane conductance; Na_t: fast inactivating sodium current; Na_p: persistent sodium current; K_t: fast inactivating potassium current; K_p: slow inactivating potassium current; SKv3.1: fast non-inactivating potassium current; SK E2: calcium-activated potassium current; Ca_{LVA}: low voltage-activated calcium current; Ca_{HVA}: high voltage-activated calcium current; I_m: muscarinic potassium current; I_h: non-specific cation current. * Density in the calcium "hot zone" between 900-1100 µm from the soma. The density of low- and high-voltage activated calcium channels in the apical dendrite was set to 1% and 10% of that value, respectively, outside of the "hot zone". ** The density of I_h in the apical dendrite increases exponentially with distance d to the soma, with parameters A = -

0.8696 pS/μm^2, B = 2.087pS/μm^2, C=3.6161, and d_{max} the distance of the apical dendrite top located the furthest from the soma. Voltage- and time-dependence of ion channels was modeled using the HH formalism. All corresponding parameters were taken from the literature and have been described in detail previously [27].

Feature	Mean ± STD	Model	Difference (STD)
Ca^{2+} AP peak	6.73 ± 2.54mV	10.8mV	1.6
Ca^{2+} AP width	37.43 ± 1.27ms	36.5ms	0.7
BAC AP count	3 ± 0	3	0
Mean somatic AP ISI	9.9 ± 0.85ms	9.4ms	0.6
Somatic AHP depth	−65 ± 4mV	-66mV	0.3
Somatic AP peak	25 ± 5mV	34mV	1.8
Somatic AP half-width	2 ± 0.5ms	1.6ms	0.8
AP count (somatic current injection only)	1 ± 0	1	0
bAP amplitude at 835µm from the soma	45 ± 10mV	14mV	3.1
bAP amplitude at 1015µm from the soma	36 ± 9.33mV	9mV	2.9

Table S2. Features of membrane potential used to constrain the intrinsic physiology of the L5PT model. Empirical features were adapted as reported previously [27]. ISI: inter-spike interval; AHP: after-hyperpolarization. Model features based on optimized parameters (see **Table S1**). Difference between model features and average experimental features given in units of STD of the experimental features. The recording locations for the bAP amplitude were adjusted to account for a longer apical trunk of the present L5PT morphology.

Presynaptic cell type	Measurement (Reference)	Network model (L5PT population)	Network model (L5PT model)
L2PY	0.08 [65]	0.06 ± 0.09*	0.13 ± 0.02
L3PY	0.12/0.55 [65, 66]	0.14 ± 0.16*	0.34 ± 0.02
L4 (SP, PY)	0.08 [65]	0.14 ± 0.16*	0.33 ± 0.04
L5IT	0.19 [67]	0.18 ± 0.13*	0.19 ± 0.05
L5PT	0.05-0.2 [67, 68, 69]	0.23 ± 0.18*	0.24 ± 0.06
L6 (BS, CT)	0.02 [65]	0.14 ± 0.15*	0.15 ± 0.02
VPM	0.44 ± 0.17 [7]	0.40 ± 0.12	0.39 ± 0.05
IN	0.22 [70]	0.41 ± 0.14	0.26 ± 0.02

Table S3. Comparison between predicted connection probabilities in wS1 network model and previously reported measurements from paired-recordings *in vitro* or *in vivo*. The * denotes predicted connection probabilities between truncated morphologies in 300 µm wide thalamocortical/semi-coronal slices of network model.

Cell type	uPSP Mean (mV) (exp. / fit)	uPSP Median (mV) (exp. / fit)	uPSP Max. (mV) (exp. / fit)	Conductance per synapse (nS)
L2PY	0.49 / 0.43	0.35 / 0.37	1.90 / 2.50	1.47
L3PY	0.49 / 0.44	0.35 / 0.39	1.90 / 1.98	1.68
L4 (SP, PY)	0.35 / 0.35	0.33 / 0.30	1.00 / 1.41	1.14
L5IT	0.47 / 0.40	0.33 / 0.35	1.25 / 1.70	1.38
L5PT	0.46 / 0.43	0.36 / 0.39	1.50 / 1.46	1.59
L6 (BS, CC)	0.44 / 0.42	0.31 / 0.40	1.80 / 1.26	1.63
L6CT	0.44 / 0.39	0.31 / 0.36	1.80 / 1.73	1.80
VPM	0.571 / 0.51	0.463 / 0.44	1.18 / 1.80	1.78

Table S4. Features of uPSP distributions of L5PTs for synaptic input from each presynaptic excitatory cell type, and the respectively fitted synaptic conductance values. Empirical values for uPSP amplitude distributions of synapses from IC cell types [61] and VPM thalamus [7] were adapted as reported previously.

https://www.dropbox.com/s/tq2kl837homq4dp/V11.mp4?dl=0

Movie S1: Examples of *in silico* pharmacology experiments.